

NATIONAL AERONAUTICS AND SPACE ADMINISTRATION

*Technical Report 32-255*

*An Experimental Correlation of the Nonreactive  
Properties of Injection Schemes and  
Combustion Effects in a Liquid-  
Propellant Rocket Engine*

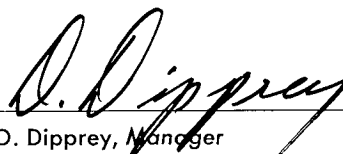
*Part II. Instrumentation, Experimental Apparatus,  
and Experimental Techniques*

*Richard M. Clayton*

*Jack H. Rupe*

*Fred G. Gerbracht*

Approved by:

A handwritten signature in dark ink, appearing to read "D. Dipprey", is written over a horizontal line.

D. Dipprey, Manager  
Liquid Propulsion Section

JET PROPULSION LABORATORY  
CALIFORNIA INSTITUTE OF TECHNOLOGY  
PASADENA, CALIFORNIA

May 15, 1967

**TECHNICAL REPORT 32-255**

Copyright © 1967  
Jet Propulsion Laboratory  
California Institute of Technology

Prepared Under Contract No. NAS 7-100  
National Aeronautics & Space Administration

## Contents

<b>I. Introduction</b>	1
<b>II. Experimental Techniques</b>	2
A. General Conditions and Operating Procedure	2
B. Apparatus	3
<b>III. Instrumentation</b>	12
A. Thermochemical Performance	13
B. Heat Transfer	16
C. Combustion Roughness	19
D. Feed System Behavior	22
<b>IV. Computational Methods</b>	23
A. Performance	23
B. Heat Transfer	24
<b>V. Analysis of Measurement and Computational Accuracy</b>	24
A. Sources of Error	24
B. Analysis of Overall Measurement Accuracy	25
<b>Nomenclature</b>	30
<b>References</b>	31

## Contents (contd)

### Tables

1. RMIR Program run series tabulation . . . . .	4
2. RMIR Program engine instrumentation location . . . . .	6
3. RMIR Program instrumentation requirements . . . . .	13

### Figures

1. Typical RMIR Program rocket engine firing; Injector 7 with $N_2O_4$ plus $N_2H_4$ . . . . .	3
2. Typical RMIR engines installed in the test stand . . . . .	5
3. Sketch of typical 20,000-lbf-thrust engine used for the RMIR Program . . . . .	8
4. ETS B Stand test facility . . . . .	10
5. Propellant valves used for the RMIR Program . . . . .	11
6. Block diagram for typical strain gage type of instrumentation channel used in the RMIR Program . . . . .	13
7. Transducer coupling-line configurations used for the RMIR Program . . . . .	14
8. Thrust calibration fixtures (in place) as used for the RMIR Program . . . . .	15
9. Digital recording equipment located in the ETS instrumentation and control center . . . . .	16
10. Thermocouple installations used for heat transfer measurements in the RMIR Program . . . . .	17
11. Block diagram for typical thermocouple instrumentation channel used in the RMIR Program . . . . .	18
12. Thermocouples installed in 43-in. $L^*$ chamber used in the RMIR Program . . . . .	18
13. Photocon shock mount used in the RMIR Program . . . . .	20
14. Analog tape recorder located in the ETS instrumentation and control center . . . . .	20
15. Block diagram for typical high-response instrumentation channel used in the RMIR Program . . . . .	21
16. Experimental performance for RMIR Injector 7 with $N_2O_4$ plus UDMH . . . . .	28

## **Abstract**

The details of the experimental apparatus, techniques, and instrumentation for an injection research program utilizing several 20,000-lbf-thrust rocket engines are given. The objectives of the program required the comparison of thermochemical performance, heat transfer, and combustion roughness behavior yielded by nine different injector designs; hence, the interest in accurate measurements was paramount. Following a description of the procedures and equipment, estimates of the achieved accuracies are presented based on a statistical analysis.



# An Experimental Correlation of the Nonreactive Properties of Injection Schemes and Combustion Effects in a Liquid-Propellant Rocket Engine

## Part II. Instrumentation, Experimental Apparatus, and Experimental Techniques

### I. Introduction

The experimental performances of a number of different liquid-propellant rocket engines have been evaluated in the course of JPL's Rocket Motor Injection Research (RMIR) Program. In an effort to demonstrate the suitability of the properties of nonreactive sprays as a basis for injector design, nine individual designs were studied, of which one was a standard *Corporal* Type I injector, an additional four were modifications of the basic *Corporal* geometry, and the remaining four were designed using the "mixing uniformity criteria" of Refs. 1 and 2. The procedures that were utilized in generating these designs and the performance levels achieved, as well as certain other injector-related phenomena, have been presented separately in Refs. 3 through 9. Consequently, only the experimental techniques and the details of the instrumentation systems are to be discussed here.

The experimental thermochemical performance for steady operation of a given liquid-propellant rocket engine can be characterized in terms of its specific impulse ( $I_s$ ) and characteristic exhaust velocity ( $c^*$ ) from the following standard relationships:

$$I_s = \frac{F}{\dot{m}_t}$$
$$c^* = \frac{A_t g_c p_{eff}}{\dot{m}_t}$$

where

$F$  = measured axial thrust

$\dot{m}_t$  = measured total mass flow rate of the propellants

$p_{eff}$  = computed nozzle stagnation pressure based on measured static chamber pressure, combustion gas composition, and chamber-to-nozzle throat contraction ratio.

$A_t$  = measured nozzle throat area

$g_c$  = constant of proportionality in Newton's second law of motion.

In view of the conventional presumption that  $c^*$  is solely dependent on processes occurring within the combustion chamber, while  $I_s$  is dependent on the chamber processes as well as flow expansion processes within the nozzle, a thrust coefficient  $C_F$  is also usually defined in an effort to separate nozzle effects from combustion effects. Thus,

$$C_F = \frac{F}{A_t p_{eff}}$$

Obviously, these several computed performance parameters are not independent, since any two of them

incorporate one or more of the same measurables. The interrelationship is usually expressed as:

$$I_s = \frac{C_F c^*}{g_c}$$

In addition to a characterization of the thermochemistry of the system, a complete performance evaluation must also include a measure of the relative difficulty of containing the combustion products and a measure of the nonsteadiness of the combustion process. In most instances, the first of these can be characterized in terms of the distribution of local heat transfer to the wall, while the latter can be expressed in terms of the time-variant pressure and/or pressure distribution within the combustion chamber.

Of course, information supplementing the engine performance measurements is also required in experimental rocket firings. This added information includes propellant tank pressures, propellant temperatures, propellant valve actuation, and injector manifold pressures, and is necessary to monitor feed system performance. In general, however, these parameters are of secondary importance (to a combustion evaluation) and some relaxation in response and accuracy requirements may be allowed.

Thus it can be seen that the overall performance of a liquid-propellant rocket engine can be determined from measurements of liquid flow rates, force, temperature, pressures (albeit of several different response capabilities), and the characteristic physical dimensions of the engine. With the exception of the pertinent dimensions, the term "measurement" is intended to include each and all of the components of the system required to obtain the analog (or digital representation) of the physical quantity of interest. Hence, the effects of coupling, transmission, and recording, as well as the unique properties of a transducer, must be accounted for in the process of deducing quantitative values from a recorded analog.

The experimental phase of the RMIR Program included the evaluation of all the previously mentioned aspects of performance for each of the injectors of interest. In the case of the thermochemical evaluations, the gross efficiency was determined over a range of mixture ratios which included the design value for the particular injector and extended far enough to either side of the experimentally determined performance peak to clearly establish a maximum. These mixture ratio surveys were repeated for each propellant combination and each  $L^*$  used with an individual injector. Enough runs were made

in each such series to allow verification of the data and reduce the ambiguity of data scatter. Performance data were taken well beyond the point in the run where steady-state conditions were achieved (most data were taken at nominally 2 sec after ignition).

Local chamber wall heat transfer rates were computed utilizing a "transient thermocouple plug" technique. Although several different geometries and "sink" materials were involved, the essential measurements in all cases were the temperature histories at two radial positions within the heat flow net for each local region of interest. Since it was not practical to install a sufficient number of thermocouples to measure the entire temperature distribution simultaneously, an array of thermocouple plugs was arranged on the chamber. Incremental variation of the orientation of the chamber with respect to the injector during a series of firings then provided the temperature distribution. The distributions were measured holding  $r$  and  $p_c$  constant at the design  $r$  of the injector/propellant combination and a  $p_c$  of 300 psia.

The nonsteadiness of the combustion process was characterized from high-response chamber pressure measurements made at the combustion chamber boundary. In most instances this measurement was located approximately 4 in. downstream of the injector face. Combustion noise (aperiodic combustion pressure fluctuations) was quantized from a measurement of the rms value of the fluctuations within a specified frequency bandwidth.

## II. Experimental Techniques

### A. General Conditions and Operating Procedure

The experimental program was conducted at Test Stand B, Edwards Test Station (ETS), Edwards Air Force Base, California. Four hundred and thirty-four short-duration (2- to 3-sec) uncooled runs of nominally 20,000-lb thrust and 300-psia chamber pressure were made during the period 7 June 1957 through 14 December 1962. A view of a typical firing is shown in Fig. 1. All of the tests were conducted at the ambient pressure of Edwards Test Station, nominally 13.5 psia (2500 ft elevation). Except for details of the individual injector face dimensions and the length of the combustion chambers, the geometrical configuration of the engines was held essentially constant for all the runs. The internal boundaries that were thus formed were nearly identical to those that had originally been designed and used in the *Corporal* propulsion system development program. Chamber sections of three different lengths could be run separately or in combination to provide nominal chamber lengths of 6,



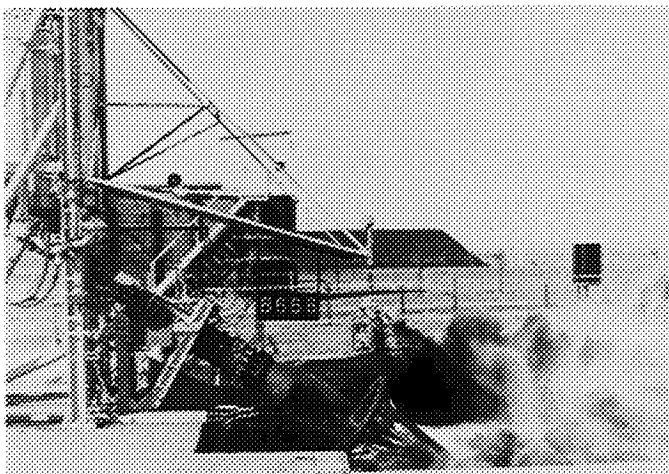


**Fig. 1. Typical RMIR Program rocket engine firing;  
Injector 7 with  $N_2O_4$  plus  $N_2H_4$  propellants**

11, 16.5 and 33 in. These various lengths provided chamber  $L^*$  values of approximately 22, 32, 43 and 78 in., respectively, the actual values depending on the particular injector used.

A gross breakdown of the runs into test series for the several propellant/injector engine combinations that were evaluated is shown in Table 1. Although the objectives of the several test series varied from configuration to configuration, the physical quantities to be determined remained relatively constant, differing only in the number of measurements to be obtained during a given run and, in certain instances, in the required accuracy.

Since the thrust level involved was relatively high, the test hardware and test firings were correspondingly expensive. In order to promote the efficiency of the test operations, a concerted effort was made to maintain standardized operational procedures. While the detailed written checklists covering the prerun stand/test hardware checkout, the firing, and post-run cleanup operations are omitted here, the salient features of these procedures can be summarized as follows:

- (1) Test stand personnel were briefed concerning the objectives of the test run or run series. Instrumentation personnel were included.
- (2) Test stand setup was made according to the above instructions. Frequent monitoring of the setup was maintained by the test conductor (engineer) who ascertained that the instrumentation and test hardware were in fact set up as directed.

- (3) After the instrumentation and mechanical setup was complete, a stand checkout was commenced. Every effort was made during the checkout to simulate run conditions so that a maximum reliability of test equipment could be achieved.
- (4) After a satisfactory instrumentation and mechanical checkout, the stand propellant tanks were filled. Pertinent procedures for bleeding instrumentation and propellant systems were included in the checklists.
- (5) Final instrumentation recorder setup was made in the recording center, and recorder calibrations were applied.
- (6) Propellant tanks were pressurized to desired pressures, and firing was made in accordance with a preset sequence-timer controller.
- (7) Test conductor recorded pertinent "quick look" data to ascertain if test conditions had been achieved.
- (8) Items 5 through 7 were repeated for each run of the day.
- (9) After the last run of the day, a stand cleanup was made.

## **B. Apparatus**

**1. Injectors.** The nine different injectors evaluated in this program (Table 1) are discussed in detail in Ref. 3 with regard to design criteria, fabrication details, and hydraulic characteristics. These details will not be repeated here. It is noted that the injector designations are those of Ref. 3 and do not necessarily imply a chronological order of design, fabrication, or testing.

The injector assemblies were provided with the structural attachments by which the engines were supported in the test stand. This arrangement permitted changing the chamber and/or nozzle assemblies without disturbing the injector or its upstream propellant valve/feed line attachments. Conversely, it allowed changing these upstream components without disturbing the relatively unwieldy engine assemblies after they had been installed on the test stand. Each injector was fitted with an identical manifold inlet port geometry so that the propellant valve connection was interchangeable. However, the position of the manifold differed in some of the installations because of the various injector designs involved. Views of these installation arrangements for typical injector/engine combinations are illustrated in Fig. 2.



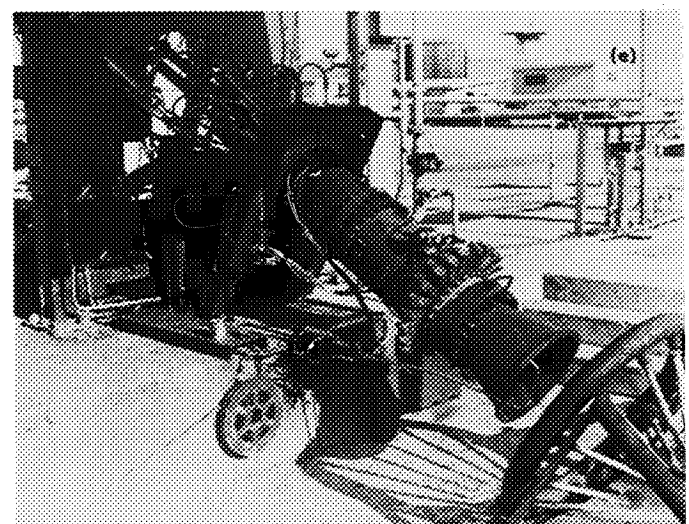
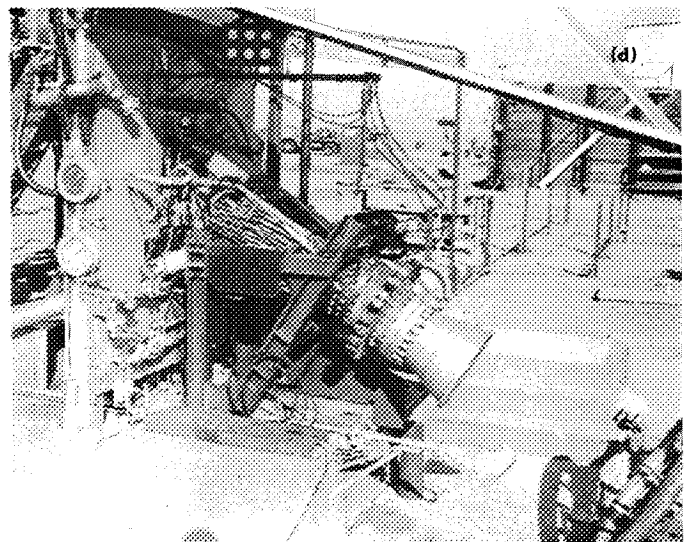
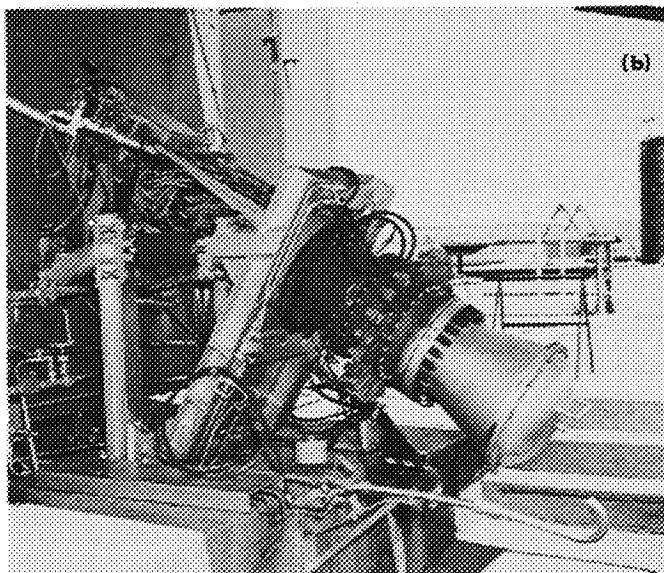
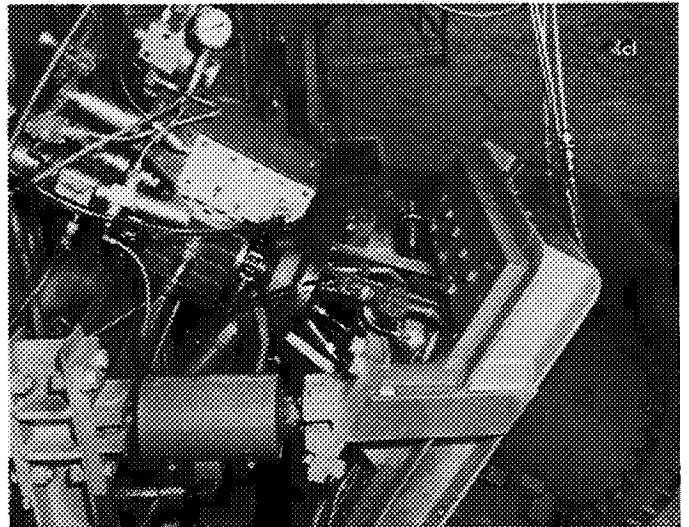
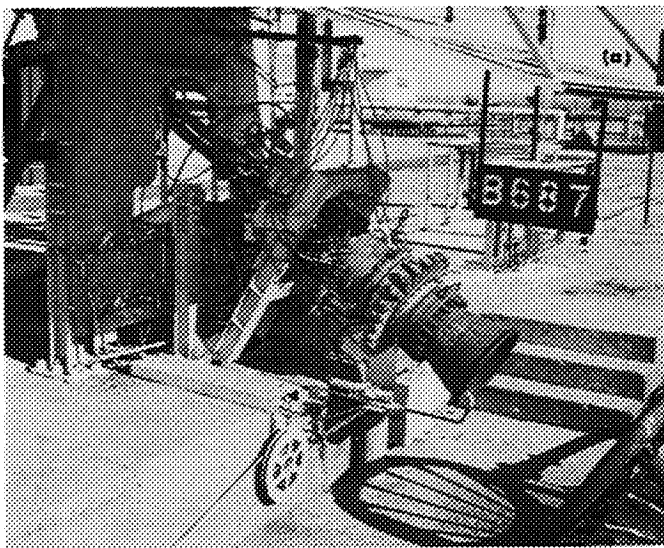


**Fig. 2. Typical RMIR Program engines installed in the test stand: (a) Injector 3 with 43-in.-L\* chamber, (b) Injector 5 with 32-in.-L\* chamber and nozzle closure plate installed, (c) Injector 6 with details of propellant valve connections to manifold shown (typical for all injectors), (d) Injector 7 with 20-in.-L\* chamber, (e) Injector 8 with 78-in.-L\* chamber.**

Table 2. RMIR Program engine instrumentation location<sup>a</sup>

	Injector									Chamber configuration L <sup>a</sup>				Nozzle <sup>b</sup>
	Corporal	1	2	3	4	5	6	7	8	43-in.	78-in.	32-in.	22-in.	
Type of measurement and parameter nomenclature	Location <sup>a</sup>													
Chamber pressure														
Injector face														
$p_{c1}$ A	11°-2.50R	11°-2.50R	11°-2.50R	11°-2.50R	11°-2.50R	75°-5.00R	15°-4.89R	72°-4.62R	30°-4.31R					
B						146°-5.00R	90°-4.89R	143°-4.75R	165°-4.31R					
C				0°-0.00R	0°-0.00R	0°-0.55R		0°-0.732R	0°-0.00R					
D						240°-4.70R	165°-4.89R	155°-5.30R	195°-4.31R					
E							195°-3.75R	305°-4.45R	293°-4.31R					
F							270°-4.89R							
Chamber wall														
$p_{c2}$ A										90°-4.00	45°-4.00	315°-3.12	315°-3.12	
B										270°-4.00	315°-4.00			
C										315°-4.00				
$p_{c3}$ A										90°-13.90	0°-31.11	30°-8.64	80°-3.72	
B										315°-13.90	135°-31.11	210°-8.64	260°-3.72	
C											315°-31.11			
Injector manifold pressure														
$p_{inj_{ox}}$														
$p_{inj_f}$														
Injector face temperature														
$T_c$ . . . . . R°						11°-2.19R 90°-2.40R	90°-3.75R 195°-4.89R 345°-4.89R	13°-2.03R 83°-2.03R 198°-3.26R	60°-3.75R 195°-2.00R 240°-3.75R					

Chamber wall temperature														
$T_c$ - - - - - °										225°-3.50	225°-3.50	45°-3.12	45°-3.12	
										225°-5.87	225°-5.87	135°-3.12	135°-3.12	
										225°-8.25	225°-8.25	195°-3.12	225°-3.12	
										225°-10.62	225°-10.62	210°-3.12		
										225°-13.00	225°-13.00	225°-3.12		
										180°-10.62	180°-10.62			
										195°-10.62	195°-10.62			
										210°-10.62	210°-10.62			
										240°-10.62	240°-10.62			
										255°-10.62	255°-10.62			
										270°-10.62	270°-10.62			
											225°-20.71			
											225°-23.08			
											225°-25.46			
											225°-27.83			
											225°-30.21			
											180°-27.83			
											195°-27.83			
										210°-27.83				
										240°-27.83				
										255°-27.83				
										270°-27.83				
Nozzle wall temperature														
$T_n$ - - - - - °														225°-0.72
														225°-2.72
														225°-4.72
														225°-6.72
														225°-8.72

\* Angular orientation referenced to clockwise displacement (as viewed looking upstream) from reference mark for respective components. Linear dimensions are in inches. (For injectors, the dimension is the radius; for chamber and nozzle it is the axial distance from the upstream end.)

<sup>b</sup> One nozzle of four used in program; others not instrumented.

<sup>c</sup> Heat transfer temperature nomenclature made up from location coordinates. Examples are: injector,  $T_c$  0110219R; chamber,  $T_c$  2251062; nozzle,  $T_n$  2250072.

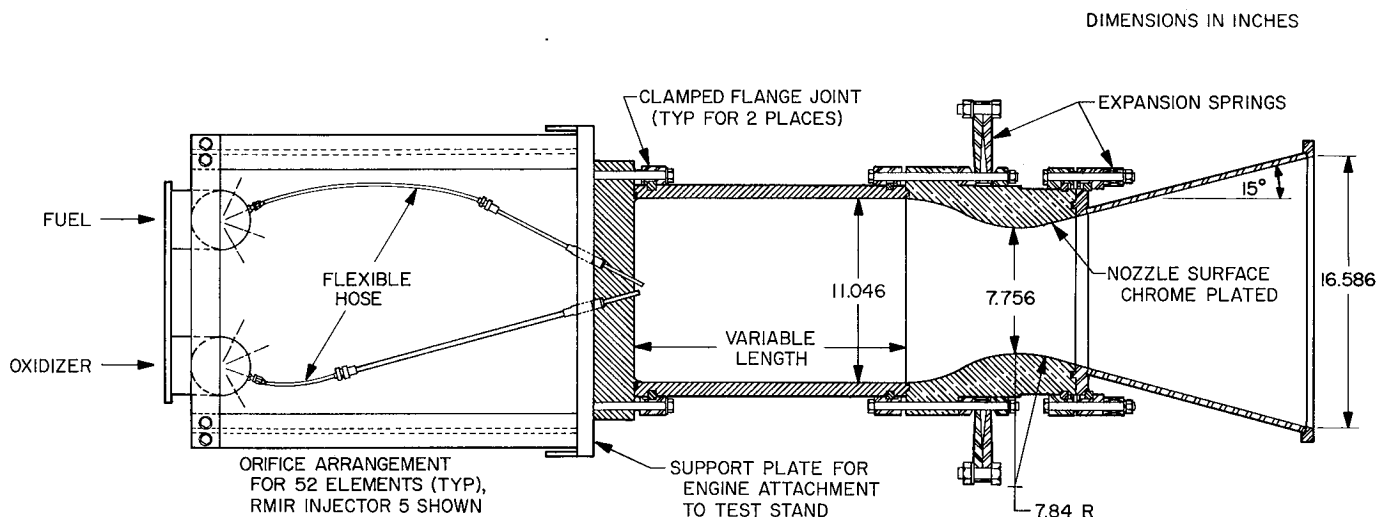
Provisions for several measurements were located on the respective injector assemblies. The types of measurements and their location are summarized in Table 2. Note that the locations of measurements on the injector face are designated with respect to an injector reference, arbitrarily chosen as the upper vertical centerline of the injector as installed on the test stand. The details of the pressure tap and thermocouple configurations are discussed in Section III.

**2. Chamber/nozzle assembly.** The various length chambers were fabricated of 12.5-in. (OD)  $\times$  11.0-in. (ID) mild steel (1020) Shelby tubing stock, machined to a finished 11.046-in. ID. This diameter in conjunction with the nozzle throat diameter of 7.756 in. produced an area contraction ratio of 2.030.

The exhaust nozzle consisted of two parts, the nozzle proper, which terminated at an expansion ratio of 1.332,

and a nozzle extension, which continued the conical expansion to an area ratio of 4.578. The nozzle was fabricated from electrolytic-copper stock, machined as shown in the sketch of the engine assembly in Fig. 3. The extension section was formed from 0.25-in. mild steel sheet stock—the 15-deg half-angle divergence extending from a tangent to the downstream throat curvature to the exit plane. This configuration resulted in a somewhat over-expanded flow (approx. 10 psia) for the propellants used and for operation at 300 psia chamber pressure.

All joints of the engine assembly were sealed by durabola gaskets and a clamped-flange arrangement. For those overall chamber lengths requiring a combination of chamber sections, an adapter ring (Fig. 2e) was inserted between the sections to provide the proper sealing arrangement. The clamped joint permitted the positioning of each component at any desired circumferential orientation.



#### ENGINE CONSTANTS

$$A_t = 47.15 \text{ in.}^2$$

$$\epsilon_\theta = 4.578$$

$$\epsilon_c = 2.030$$

$$(C_F)_{exp} = 1.410 \quad \lambda C_d = 1.362$$

#### ASSUMING:

$$\gamma = 1.25$$

$$p_c = 300 \text{ psia}$$

$$p_a = 13.5 \text{ psia}$$

$$\lambda = 0.984 \text{ (15 deg)}$$

$$C_d = 0.985$$

$$F = 19,300 \text{ lbf}$$

#### $L^*$ VALUES FOR THE VARIOUS RMIR ENGINE CONFIGURATIONS

INJECTORS	NOMINAL $L^*$ , in.			
	78	43	32	22
<i>CORPORAL</i> AND 1-4	—	40.7	—	—
5	77.9	43.0	32.3	22.3
6	77.4	42.5	—	—
7	77.4	42.5	—	21.8
8	79.1	44.2	—	—

Fig. 3. Sketch of typical 20,000-lbf-thrust engine used for RMIR Program

Reference marks on each component provided the necessary orientation correlations. In order to compensate for the differential thermal expansion between the copper and steel parts, spring-loaded flange bolts were incorporated at the chamber-to-nozzle and nozzle-to-extension joints. This arrangement maintained a relatively constant gasket compression force throughout a firing. A flange was also provided at the exit end of the nozzle extension which allowed closure of the engine assembly for leak testing. These various features are illustrated in Figs. 2 and 3.

In a manner analogous to the injector instrumentation designations, all chamber and nozzle instrumentation locations were designated relative to the respective reference marks for each component. These locations are summarized in Table 2.

**3. Test stand.** The test stand utilized during the program was a short-duration static test facility of 50,000-lbf-thrust capacity, incorporating a gas-pressurized propellant feed system, electromechanical remote control system, thrust measuring system, propellant storage and transfer system, and a transducer cooling system utilizing distilled water as a working fluid, as well as the usual flame-pit cooling and fire-fighting water deluge systems. The facility was connected to the ETS Instrumentation and Control Center (located at a distance of 450 ft from the test stand) by a 7-ft-diameter tunnel through which all instrumentation and control circuit cabling was routed. General views of the test stand area, tunnel, and the B Stand area of the Control Center are shown in Fig. 4.

Gaseous  $N_2$  was supplied to the propellant tanks from the ETS high-pressure storage system. Pressure reduction to appropriate levels was accomplished by means of standard pressure regulation schemes through regulators located at the tank-pressurant inlets. Fuel and oxidizer tanks (of 30- and 50-gal capacity, respectively, and fabricated of 18-8 stainless steel for a working pressure of 1000 psi) supplied propellant flow through flowmeters, feed lines and the propellant valve to the injector manifolds. Propellants were transferred to these run tanks from a ready-storage system which allowed efficient fill and drain-back operations.

Venturi flowmeters fitted to the propellant outlet of each tank furnished the primary flow measurement for this program. The large diameter of the tanks relative to the venturi throat diameter, the incorporation of anti-swirl vanes across the outlet end of tanks, and the use of pressurant-gas flow diffusers provided adequately controlled inlet conditions to the venturi meters.

Secondary or backup flow measurements were obtained from turbine flowmeters located at the inlet ports of the propellant valve. In order to provide flexibility to the feed lines interconnecting the flow measurement devices, and thus to accommodate the valve locations dictated by the different injector designs, each feed system was fitted with a 4.5-ft-long section of 1.5-in.-D teflon-lined hose (Fig. 4b). A transition from this hose size to the 2.5-in. turbine meters, as well as a necessary 90-deg change of flow direction, was obtained by a combination vaned turn/flow straightener assembly. The net result of this arrangement was that nearly fully developed turbulent flow was produced at the entrance to the turbine meters without sacrificing the flexibility and compactness of the feed system.

The term "propellant valve" as used herein refers to the valve in the propellant feed system through which the entire propellant flow passed and by which the starting and termination flow transients were controlled. All of the early runs of the program were made with nearly identical versions of the so-called *Corporal* propellant valve. This valve assembly is shown installed in the test stand with RMIR Injector 5 in Fig. 5a and consisted of two individual blade valves of unequal size, mounted together and operated by a common pneumatic actuating cylinder. The opening rate of the valve was determined by the rate of the actuating piston travel which was controlled by a gear-driven lead-screw/rotating-nut arrangement. Nominal opening times of 1, 2, 3, and 4 sec were available through the proper selection of gear ratios. The closing rate of the valve was determined by the venting rate of the opening side of the actuating cylinder. Since the oxidizer blade was wider than the seat diameter, some adjustments of the mechanical "lead" of the valve were possible by varying the initial (closed) position of this blade on its seat. However, both the opening time and lead adjustments were fixed when the valve was assembled, so that any readjustments required partial disassembly of the valve. Furthermore, for those situations requiring valve closure prior to propellant exhaustion, the dynamic forces imposed a cantilevered load on the valve blade which resulted in gouging the teflon seals with subsequent leakage past the seat. As the program progressed, it became obvious that a more durable valve was required as well as a more convenient method to provide valve-lead and opening-rate adjustments. In short, a propellant valve tailored to test stand operation was necessary.

To this end, a dual ball valve<sup>1</sup> was selected which consisted of two identical individual valves mounted together

<sup>1</sup>Manufactured by Hydromatics, Inc., Bloomfield, New Jersey.



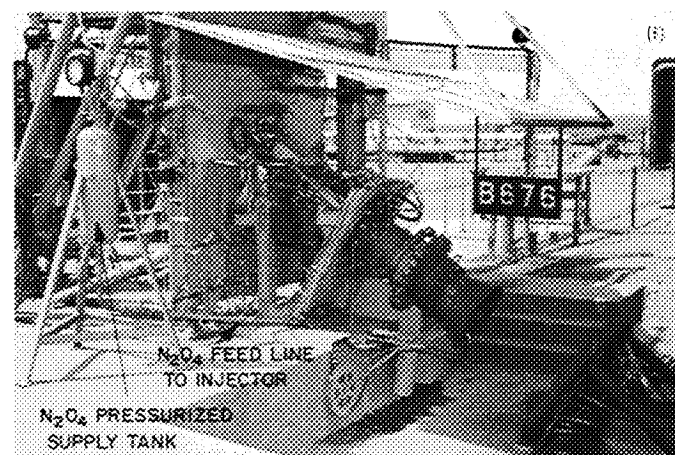
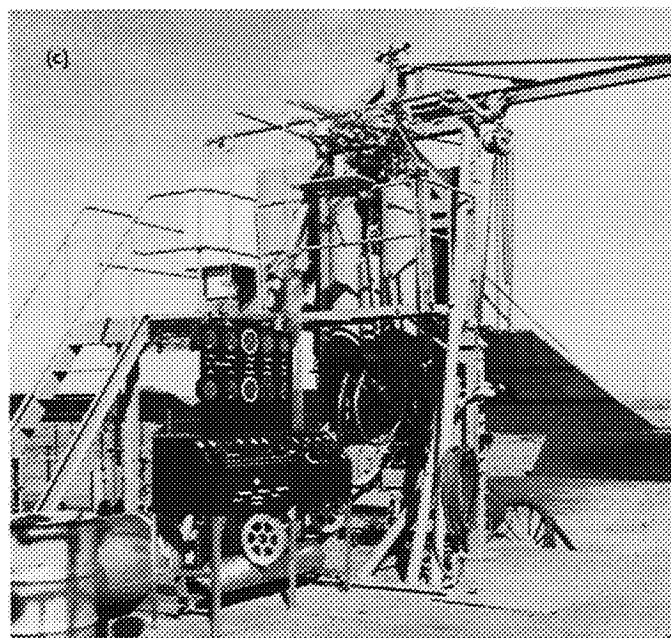
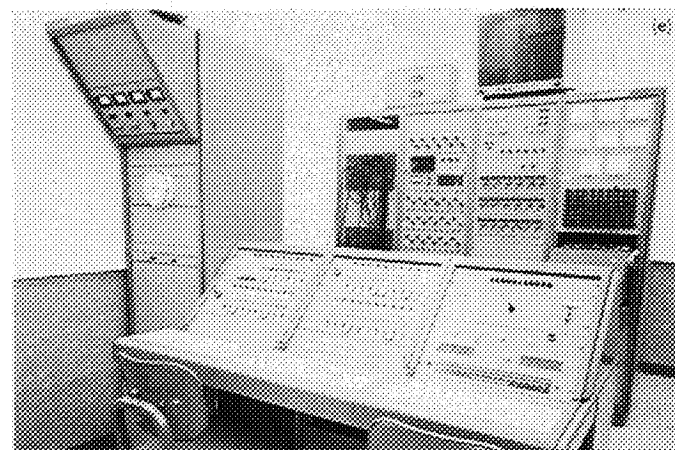
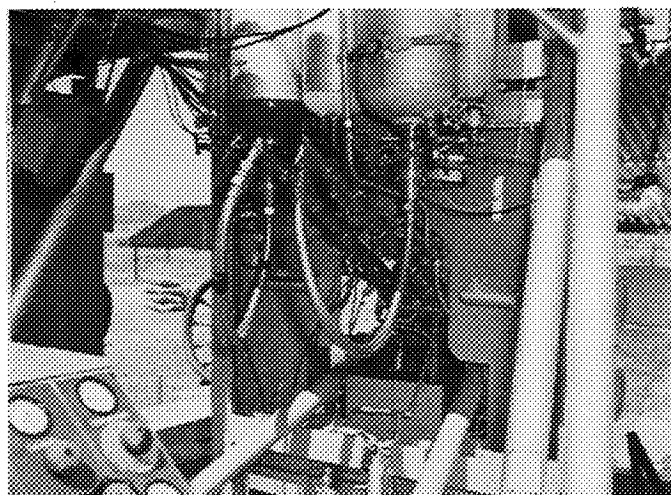
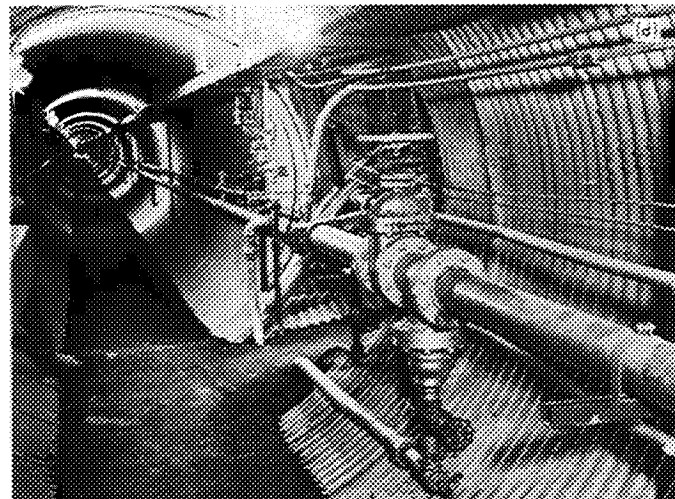
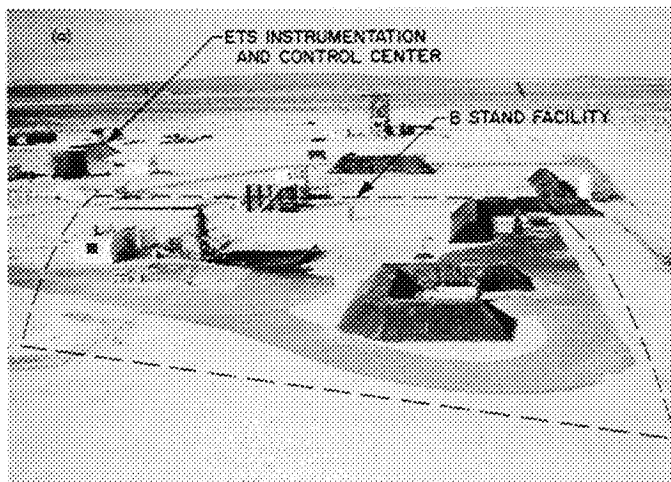
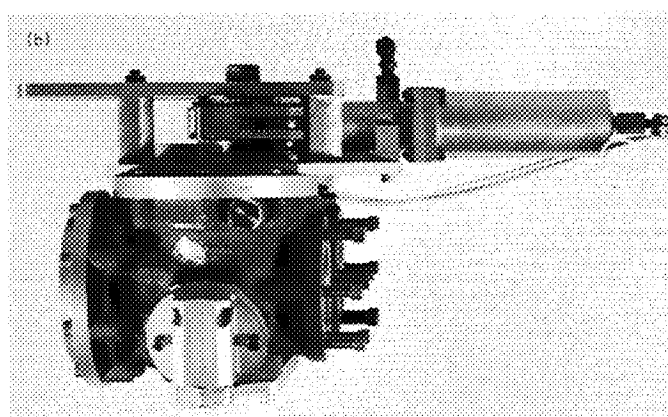
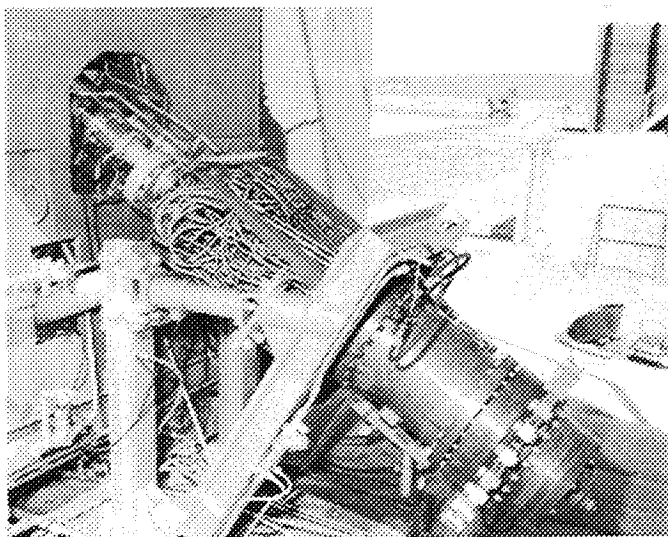


Fig. 4. ETS B Stand test facility: (a) overall view, (b) typical propellant feed line installation, (c) backside view showing propellant transfer control panel, (d) tunnel connecting test stand and control center, (e) B Stand control console located in the ETS control center, (f) N<sub>2</sub>O<sub>4</sub> starting system utilized for pentaborane/hydrazine tests





**Fig. 5. Propellant valves used for RMIR Program:**  
**(a) Corporal blade valve as installed for early**  
**tests on Injector 5 (run B465), (b) hydromatics**  
**ball valve assembly (dust cover removed)**  
**after linkage modification by JPL**

rigidly, a common actuating cylinder, and an interconnecting operating mechanism. The original operating mechanism was redesigned at JPL to provide a lead adjustment which was continuously variable over a range of 30 deg (ball rotation) for either ball relative to the other and a continuously variable opening time through a practical range of 30 msec to 4 sec. A view of the assembly is shown in Fig. 5b. A detailed discussion of the mechanical and hydraulic characteristics of this valve, together with a description of its electropneumatic control system, is presented in Ref. 7. As noted therein, the essential operating requirements for this valve included a relatively slow opening and a fast closure, the former dictated by starting transient considerations and the latter by the necessity of terminating the run as quickly as

possible in the event of an intolerable combustion mode. With respect to the latter, it was found that closure times of nominally 50 msec would provide adequate protection and, at the same time, limit dynamic effects in the upstream system to tolerable levels.

Although this valve proved to be reliable and durable, some operational difficulties were encountered. The first was caused by the use of a water flush through the oxidizer injector manifold following each day's operation. Residual SFNA/water mixture was sufficient to cause a salt formation on the exposed downstream surface of the aluminum ball so that given a day or so of idleness to collect the salts, the valve seat (teflon) would be damaged during the next operation of the valve. (This problem was alleviated when  $N_2O_4$  was used.) The salting was reduced by eliminating the water flush. The SFNA also attacked the 440C bearing material and necessitated its replacement about every three weeks while the acid was used. The expense of better bearing material was not justified, however, owing to the ease of replacing the 440C bearings at relatively low cost. Finally, it became apparent that the corrosion rate of the aluminum used in the construction of the original oxidizer valve assembly, when used with SFNA, was too high for long-term use. Therefore, the parts for one ball assembly were fabricated of stainless steel (Types 321 and 17-4 PH) and installed in the oxidizer system, thereby eliminating the corrosion and pitting problems.

A gas-pressurized, distilled-water supply system was used for cooling the high-response pressure transducers<sup>2</sup> for all tests through run B791. The system consisted of a pressurized tank supply, inlet and outlet distribution manifolds for connecting several transducers, a back pressure regulator, and a return tank. For runs subsequent to B791, a recirculating pump system was used which comprised a 70-gal tank, a two-stage centrifugal pump, and inlet and outlet distribution manifolds. Pressure disturbances introduced by the pump were reduced to insignificantly low levels by maintaining an approximate 90-in.<sup>3</sup> air cavity in the top section of the inlet distribution manifold.

It is noted that in addition to providing the required coolant flow rate, these systems had a second essential function: viz., to maintain the pressure level in the coolant passage at a value greater than mean chamber pressure. Thus, in the event of rupture or burnout of the external diaphragm, the flow of hot chamber gas through the trans-

<sup>2</sup>Manufactured by Photocon Research Products, Pasadena, California.

ducer was prevented, allowing only partial failure of the transducer and preventing destruction of the hardware on which it was mounted. In most instances when such a failure occurred, the transducer was salvable at approximately half-replacement cost and little or no damage was sustained by the mounting. It should further be noted that Photocon Research Products does not recommend the use of high-pressure coolant water. However, experiments at JPL have shown that certain models (352 and 307, for instance) can tolerate cooling pressures as high as the rating of the gage and that the most serious effect on operating characteristics is a "zero" shift.

The control of engine firings (i.e., propellant tank pressurization vent valves, injector flush valves, propellant valve, etc.) was accomplished remotely from a console (Fig. 4d) located in the Instrumentation and Control Center. In addition to the remote controls for stand operation, the console was also equipped with a communications system that was interconnected with the stand, the station safety tower, and the appropriate instrumentation recording stations.

Functions which were controlled locally at the stand were those associated with prerun checkout, propellant transfer, and postrun cleanup of the stand. A control panel for this purpose was located at the stand and is shown in Fig. 4c.

For the test series involving the pentaborane/hydrazine propellants (Table 1), it was necessary to revise what was normally the oxidizer system of the stand to provide complete isolation of the pyrophoric pentaborane from contact with air. In addition, it was necessary to incorporate a vent scrubber for that system in order to neutralize the toxic fumes. Finally, a hydrocarbon flushing system was required to flush the residual  $B_5H_9$  from the propellant system following each test. Because none of these modifications influenced the essential features of the feed system with regard to the propellant flow for the engine firings, and since the revisions followed standard practice in handling  $B_5H_9$ , no attempt is made here to detail the changes. Suffice it to say that the substitution of a pyrophoric propellant for "normal" propellants on a relatively large-scale rocket test stand added complication to the operating procedures, but it was not of sufficient significance to seriously curtail the testing schedule.

Since the pentaborane was not sufficiently hypergolic with the  $N_2H_4$  to insure reliable ignition, a start-slug system utilizing  $N_2O_4$  was added to the test stand. The  $N_2O_4$  was supplied from an ancillary gas-pressurized feed sys-

tem (Fig. 4e) and injected through two spray nozzles installed on the face of the injector. The selection of the proper  $N_2O_4$  feed tank pressure together with the properly sequenced opening of the  $N_2O_4$  flow control valve provided an  $N_2O_4$  injected flow rate of approximately 10% of the total propellant flow rate. This flow commenced nearly simultaneously with the main propellant injection and continued until design chamber pressure was attained. A check valve prevented reverse flow whenever chamber pressure exceeded the  $N_2O_4$  feed tank pressure. Further details of the pentaborane test series and the results obtained are discussed in Ref. 9.

### III. Instrumentation

As was indicated in Sections I and II, the physical parameters of interest to the program included *pressure*, *temperature*, *force* and *flow rates*, as well as *time*, with each or all of these being determined for various reasons and at various locations on the test hardware. Since it is clear that even the "steady state" combustion process is not truly steady in time, the determination of such gross performance indexes as  $c^*$  and  $I_s$  is meaningful only when they accurately represent some sort of known time-average value. Yet, the averaging time cannot be too long, for in the case of short-duration firings the measurements would include effects due to the engine starting transient, and in any case the several measurements used for performance calculations should be identically capable of precisely following "slowly" changing engine variables. The same comments are generally true for heat transfer measurements. The characterization of combustion roughness, however, requires even higher response capabilities because of the rapid transient nature of the dynamic phenomena associated with combustion processes. Unfortunately, the overall accuracy of high-response measurement systems ( $>1000$  Hz) is usually poor compared to that for systems with relatively long time constants ( $<100$  Hz), so that they are not always interchangeable from this standpoint. Thus, it can be seen that the specifications for particular measurement techniques are dominated by attempts to generate true time history analogs of the monitored parameters, but may include compromises in maximum response capability to accommodate achievement of the desired accuracy.

In order to discuss the measurements made in this program, it is convenient to group the parameters in accordance with the intended category of engine behavior to be deduced: namely (1) thermochemical performance, (2) heat transfer, (3) combustion roughness, and (4) feed system behavior. The parameters are tabulated in this manner

**Table 3. RMIR Program instrumentation requirements**

Measurement category	Parameters and nomenclature	Desired characteristics	
		Response, Hz	Accuracy, <sup>a</sup> %
Thermochemical performance	Head end chamber pressure $p_{c1}$	0-100	$\pm 1/4$ or better
	Nozzle entrance chamber pressure $p_{c5}$	↓	↓
	Flow rates; venturi $(\Delta p)_{ox, f}$ or turbine meter (FM) $_{ox, f}$	↓	↓
	Thrust $F$	↓	↓
	Propellant temperature $(T)_{ox, f}$	0-100	↓
	Atmospheric pressure $p_a$	—	$\pm 1/4$ or better
Heat transfer	Inner (recessed) and outer wall temperature $T_w$	0-1000	$\pm 2$
Combustion roughness	High-response pressure at chamber boundary $p_{c2}$	0-10,000	$\pm 10$
Feed system behavior	Propellant tank pressure $(p_t)_{ox, f}$	0-100	$\pm 5$
	Injector manifold pressure $(p_{inj})_{ox, f}$	0-1000	$\pm 5$
	Propellant valve ball opening position	—	—

<sup>a</sup>Assumed  $2\sigma$  confidence level.

in Table 3, where the desired overall accuracy and response characteristics of the various measurements are also listed.

#### A. Thermochemical Performance

The basic performance measurements were chamber pressure, flow rates, and thrust, while supplementary measurements were propellant temperatures and atmos-

pheric pressure. The basic measurements (with the exception of the turbine meter flow measurement) were all obtained using various strain-gage-type transducers. Figure 6 illustrates a block diagram of a typical channel of this kind of instrumentation. Also depicted are several sources of error ( $e_1, e_2, \dots, e_7$ ) for this class of measurement which will be evaluated in Section V.

Although unbonded strain element pressure transducers<sup>3</sup> were used for chamber pressure measurements in early tests, bonded element transducers<sup>4</sup> were utilized almost exclusively for chamber pressure in firings subsequent to B445. Owing to a similar evolution of transducer development, the Foxboro  $\Delta p$  transducers<sup>5</sup> originally used for venturi meter measurement were replaced by Satham  $\Delta p$  transducers at this same time.

Since it was necessary to connect these transducers to the pressure source by means of pressure taps and coupling lines, and since the measurement error from uncontrolled averaging characteristics of coupling lines can be large, the coupling configuration was important with regard not only to the dynamic response but also to the accuracy of the measurement. For this reason, a continuous effort to improve and define coupling line dynamic characteristics was carried out by JPL's Instrumentation Section (Ref. 10). The configurations and corresponding response characteristics shown in Fig. 7 are typical of the results of this effort as applied to the RMIR Program.

Note that the response of all these configurations falls short of the 100 Hz (Table 3) which was desired. It is believed, however, that the response obtained is essentially the practical limit for these systems, considering the

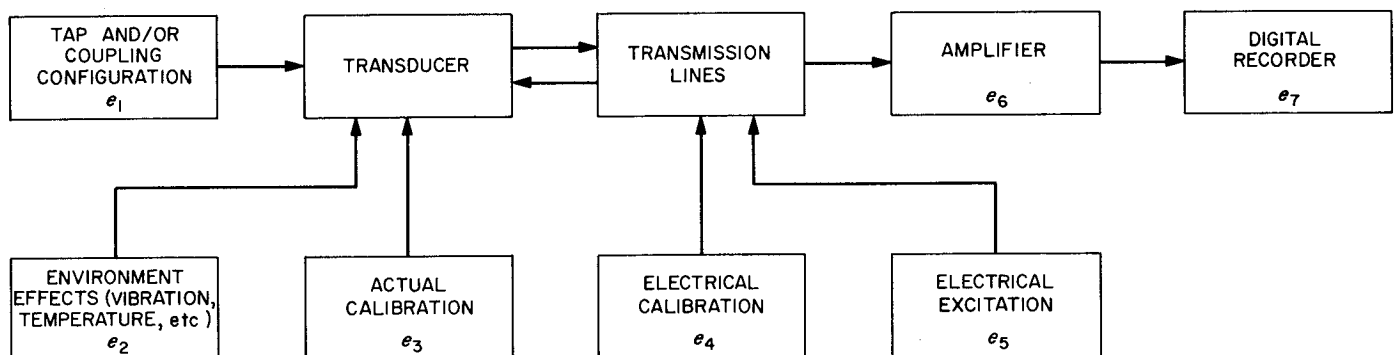


**Fig. 6. Block diagram for typical strain-gage type of instrumentation channel used in RMIR Program**

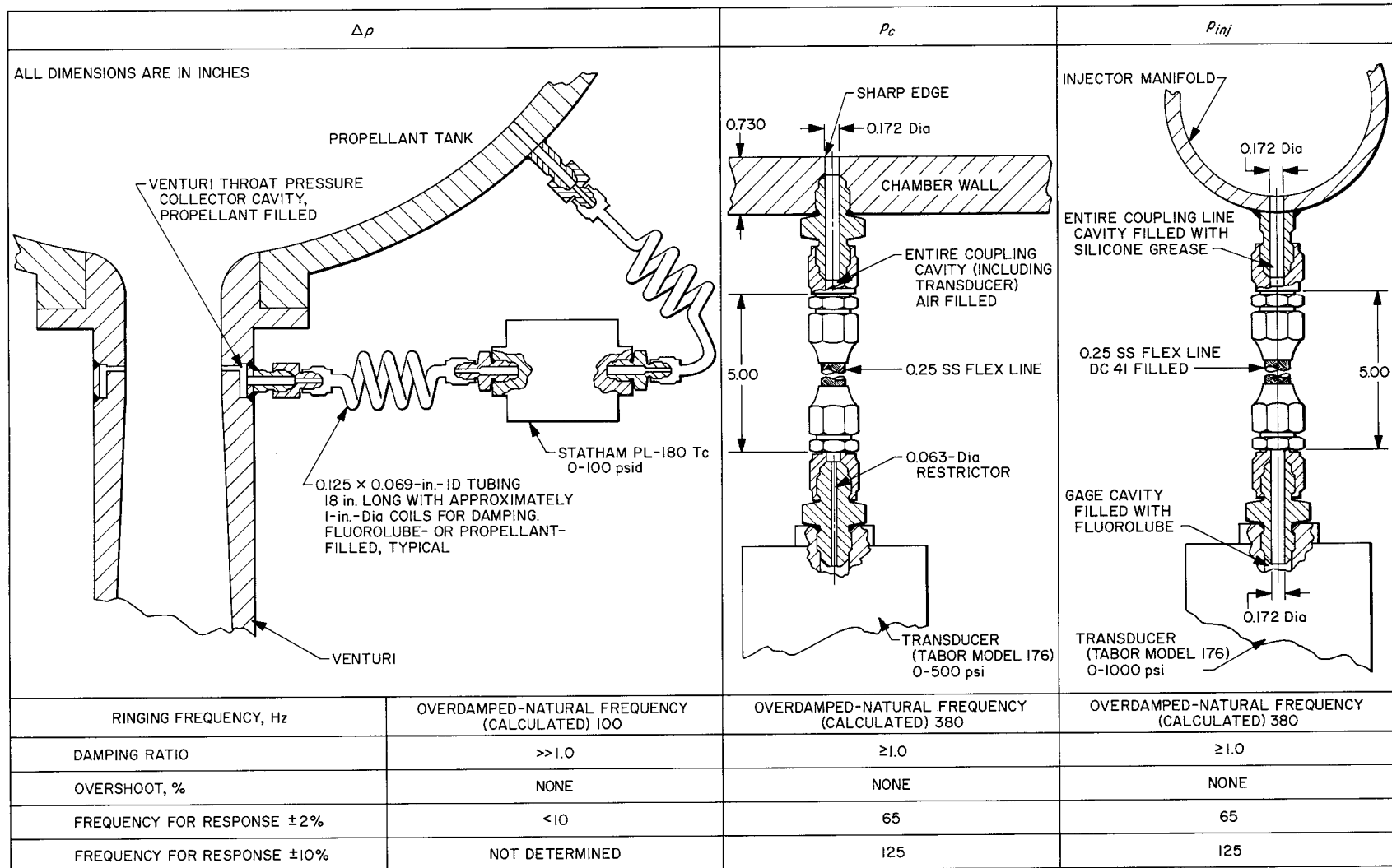


Fig. 7. Transducer coupling-line configurations used for RMIR Program

cavity volume associated with the transducer and connecting configuration for conventional strain-gage pressure measurements. In the case of the venturi  $\Delta p$  measurements, a particularly poor response situation existed. Here, the venturi throat pressure tap comprised a complicated hydraulic passageway, but of more importance was the exceptionally large cavity volume change with pressure for the  $\Delta p$  transducers. In order to control the incipient resonance exhibited by this coupling line/cavity configuration, it was necessary to incorporate damping by using relatively long, small-diameter lines coiled as shown in Fig. 7. Even so, the response of this Statham  $\Delta p$  arrangement was several times better than the best that could be obtained with the original Foxboro transducers.

Static pressure calibrations were performed on these pressure parameters using a bourdon tube gage<sup>6</sup> as the reference standard. The working fluid of gaseous  $N_2$  was controlled by hand-operated pressure regulators. The use of this pneumatic system reduced the problem of contamination of transducer cavities and coupling lines which were to be exposed to highly reactive propellants. To verify their validity, calibrations were repeated frequently, every three or four firings or whenever the data were obviously questionable.

The thrust measuring system consisted of a hinged thrust plate to which the engine was mounted. Two load cells, acting in parallel and placed on either side of the thrust plate so as to straddle the thrust vector, restrained the plate from rotation about the hinges. The load cells were updated for runs subsequent to B530, when the original JPL-fabricated non-temperature-compensated cells were replaced with Baldwin units.<sup>7</sup> The response characteristics of the thrust measuring system were never accurately evaluated, but it is estimated that they, like the venturi  $\Delta p$  measurements, fell far short of the desired 100-Hz response since the system appeared to have a resonant frequency of approximately 60 Hz. Thrust calibrations were performed by generating the calibration loads with a hydraulic jack and applying these forces (through a tandemly mounted reference-standard load cell) to the exit plane of the nozzle along the centerline of the engine (the assumed position of the thrust vector). Engine and test stand plumbing was connected in run configuration for the calibrations. The fixtures used for calibration are illustrated in Fig. 8.

<sup>6</sup>Manufactured by Heise Bourdon Tube Co., Newtown, Connecticut.

<sup>7</sup>Manufactured by Baldwin-Lima-Hamilton Corp., Waltham, Massachusetts.

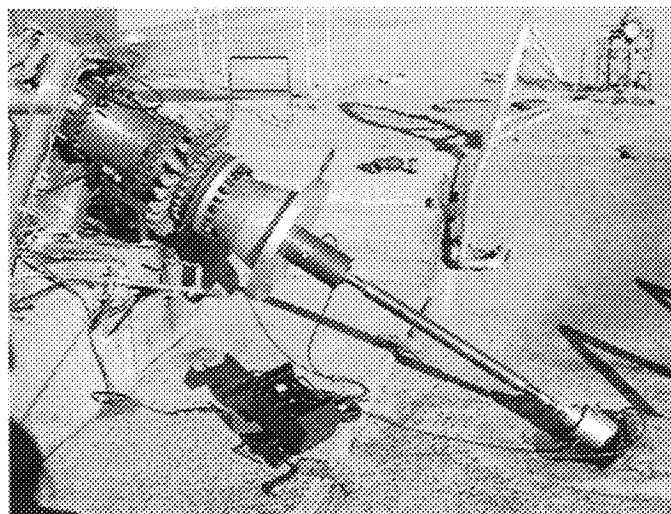


**Fig. 8. Thrust calibration fixtures (in place) as used for the RMIR Program**

The use of turbine flowmeters for the previously mentioned backup flow measurement commenced with Run B472. Waugh flowmeters<sup>8</sup> with 400-pulse/sec maximum frequency output were used through Run B536. The meters were then modified for ball bearings of 17-4 PH stainless-steel material and an increased frequency output to 2000 pulse/sec maximum.

Both the venturi and turbine flowmeters were calibrated frequently with water. Special calibration tanks, geometrically identical to the stand run tanks, were used for the venturi calibrations.

Turbine meter calibrations were usually performed simultaneously with the venturi meters, using the actual test stand feed line components (flexlines, vaned elbows, flow-straightening sections) installed downstream of the venturi. Alternatively, the turbine meter calibrations were obtained using a 20-diameter straight approach section in lieu of the feed line components.

Propellant temperatures were measured by thermocouple probes inserted to a depth of several inches from the bottom of the respective run tanks. The probes consisted of copper-constantan encased in 1/8-in.-OD stainless-steel tubing sealed to withstand the tank pressure. The probe thermocouples were referenced to a 32°F ice junction.

<sup>8</sup>Manufactured by Waugh Engineering Division of The Foxboro Co., Van Nuys, California.

Performance data from the foregoing transduction systems were recorded on Leeds and Northrup<sup>9</sup> (Speedo-max) and Honeywell<sup>10</sup> (Brown) direct-inking strip chart recorders through Run B664. For subsequent runs, only "quick look" performance data were recorded in this manner. Commencing with Run B665, all performance parameters were digitally recorded.

The high-speed digital data system was a MicroSADIC unit.<sup>11</sup> The data were recorded on magnetic tape in a bipolar-binary-coded-decimal blocked format and were compatible with the input requirements of either the IBM 704 or 7090 digital computers. Each parameter was sampled nominally 56 times/sec, the actual rate being governed by the total number of parameters being digitized.

Several channels of pulse counters were also connected to the MicroSADIC to permit sampling and recording (at the above rate) the accumulating number of pulses from the turbine flow meters as the run progressed. The time rate of accumulation, and hence meter output frequency, was subsequently computed during the data reduction routines.

Typical views of the digital recording equipment, which was located in the ETS Instrumentation and Control Center, are shown in Fig. 9.

## B. Heat Transfer

A transient thermocouple plug technique described in Ref. 11 was used to determine the local heat flux through the chamber wall, nozzle wall, and injector face. The method requires the measurement of the temperature histories at two radial positions within the heat-conducting material and along the heat path (direction assumed to be normal to the hot-gas-side surface) for each local region of interest. In order to minimize errors associated with the determination of the temperature gradient at the inner surface, it is desirable to measure the surface temperature directly and, as indicated in Ref. 11, this is sometimes done. However, as the technique was applied in this program, the innermost wall thermocouple junction (the so-called recessed thermocouple) was nearly always recessed 0.020 in. because it was deemed essential to protect this junction from the corrosive environment of the reactants.

<sup>9</sup>Philadelphia, Pennsylvania.

<sup>10</sup>Denver, Colorado.

<sup>11</sup>Manufactured by Consolidated Systems Corp., Monrovia, California.

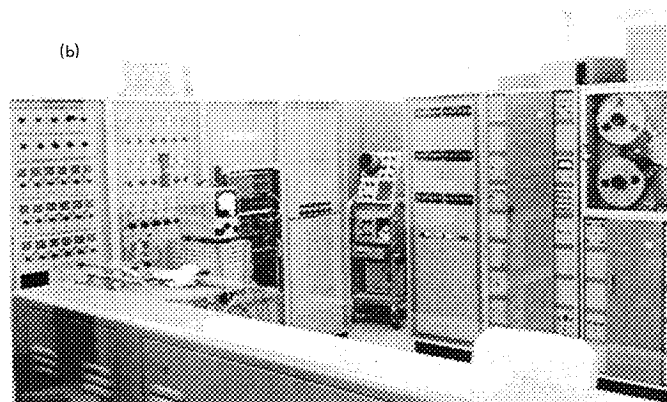


**Fig. 9. Digital recording equipment located in the ETS instrumentation and control center: (a) instrumentation control console, (b) overall view of digital recording equipment**

The second thermocouple of each pair was positioned on the outer (cold) surface of the respective wall of interest as nearly in line with the recessed junction as practical. Although the alignment of these two junctions was not exact, as the computational model required, the results were unaffected since the outer wall temperature was essentially constant during a typical firing. This was a consequence of the thick walls and the normally short run durations (generally less than 3 sec).

Two types of thermocouple plugs, a pressed-in JPL design and a commercially available threaded design,<sup>12</sup> were used interchangeably (insofar as function is concerned) in the injector face and chamber wall. Sketches of these configurations are shown in the upper part of

<sup>12</sup>Delta-Couple, manufactured by Advanced Technology Laboratories, Mountain View, California.

Fig. 10. In either case, the plugs were made of the same material as the walls in order to minimize disturbances to the heat flow caused by variations in specific heat and thermal conductivity. Chromel-alumel thermocouple materials were used for all junctions and lead wires. A block diagram of a typical thermocouple circuit is shown in Fig. 11.

During the latter phases of the program the screw-in configuration was used almost exclusively. This design was used in order to obtain a more rugged thermocouple junction, since the welded joint utilized in the press-in plug proved to be susceptible to failure—particularly as a consequence of rough combustion. The Delta-Couple junction was formed by electroplating approximately

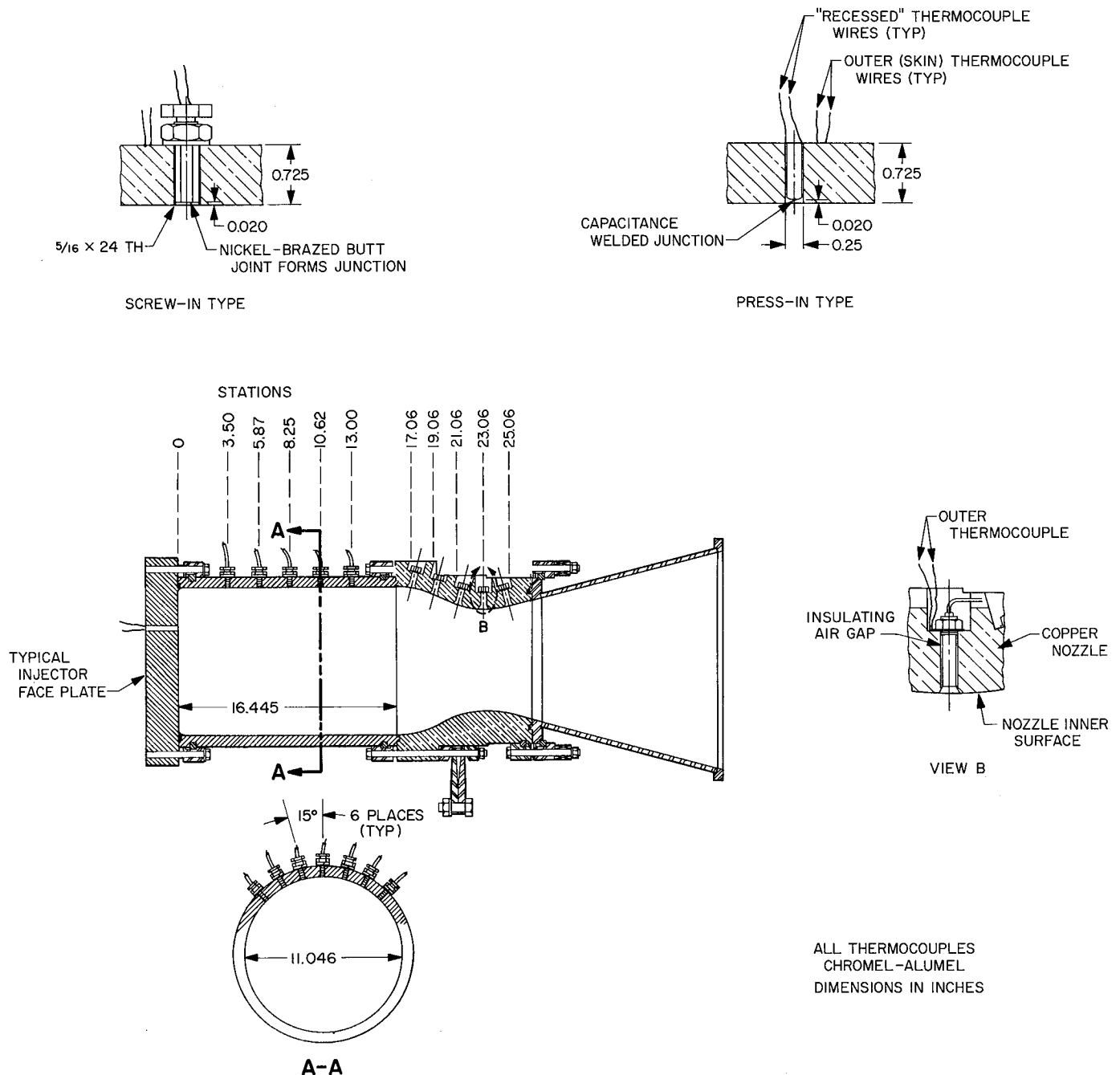


Fig. 10. Thermocouple installations used for heat transfer measurements in RMIR Program

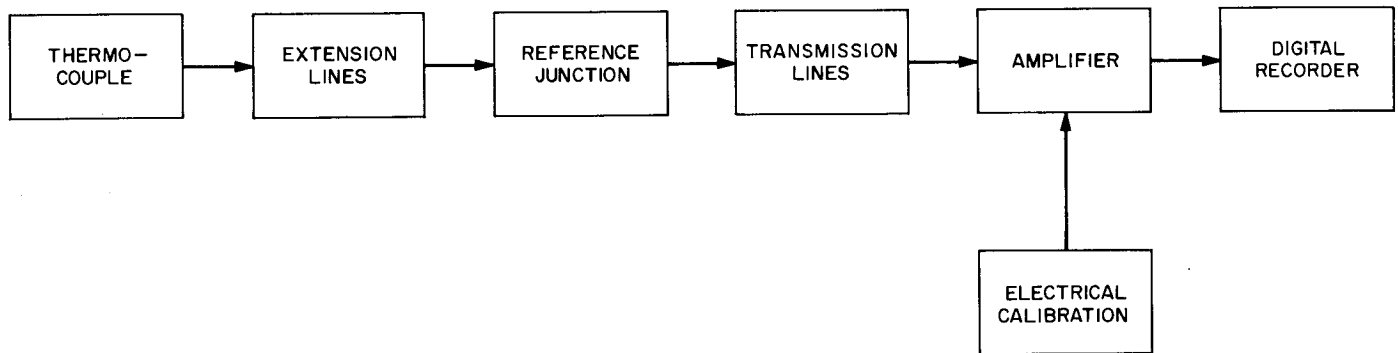


Fig. 11. Block diagram for typical thermocouple instrumentation channel used in RMIR Program

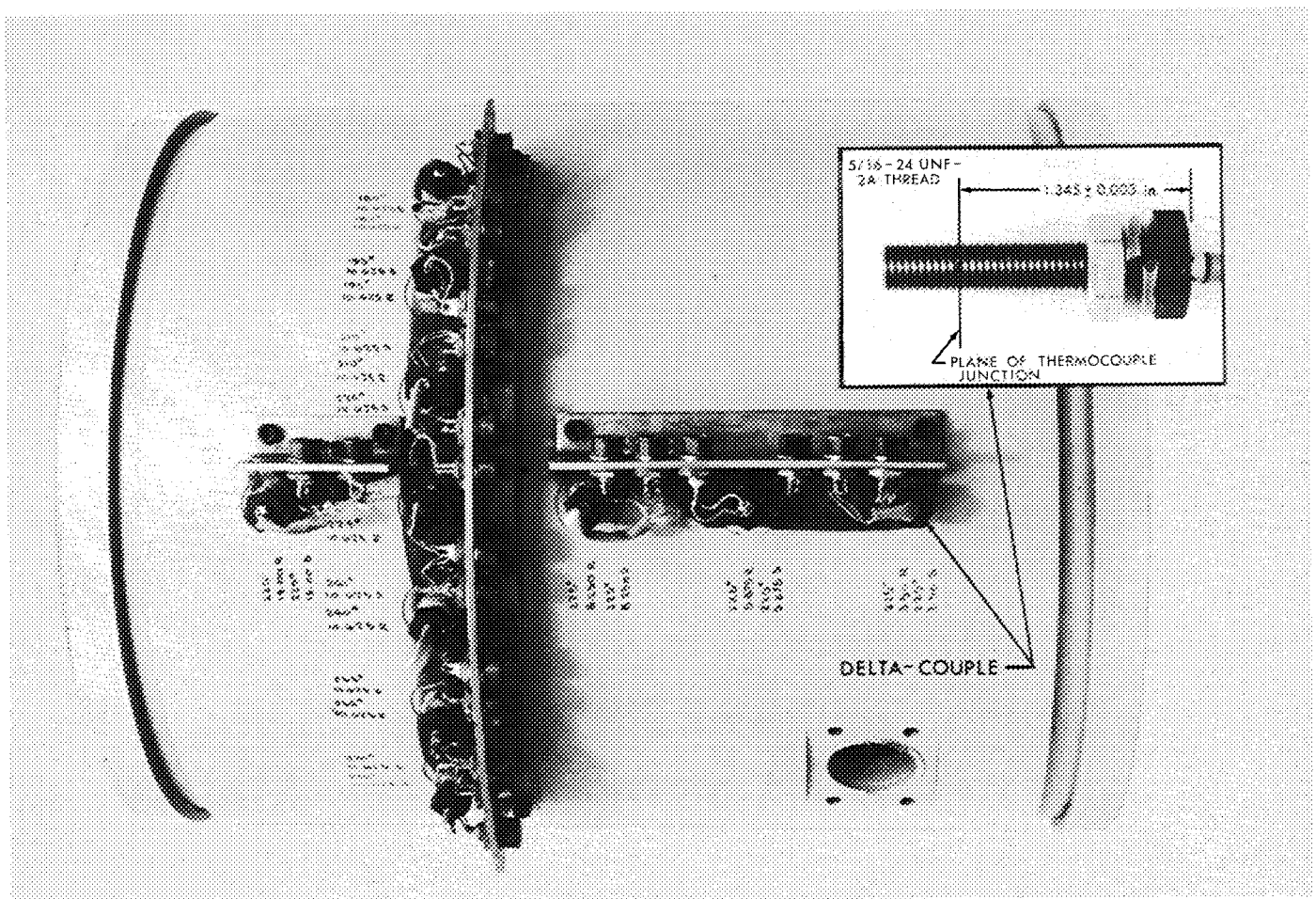


Fig. 12. Thermocouples installed in 43-in.-L\* chamber used in RMIR Program

0.003 in. of copper over the ends of the thermocouple leads as swaged into the parent plug material and then brazing an extension to that joint. The "rough" plug could then be turned and threaded (see inset, Fig. 12) and the position of the junction determined by X-ray inspection.

Although the thread could modify the measurement compared to an ideal measurement arrangement which does not introduce varying thermal resistances due to installation interfaces, such errors were considered negligible relative to those introduced by the assumption, required



by the computer analysis, that axial and circumferential temperature gradients within the chamber walls are negligible. In summary, the screw-in configuration was significantly easier to install initially, was replaceable in the test stand, and indeed did prove to be a much more rugged assembly than the press-in plug design.

The geometrical array of thermocouples utilized for most of the chamber heat transfer measurements is illustrated schematically in Fig. 10 for the 43-in.- $L^*$  chamber. A view of the external appearance of the chamber wall thermocouples is shown in Fig. 12. Note that locations used for the other  $L^*$  chambers are tabulated in Table 2.

For the few runs in which nozzle heat transfer temperature measurements were attempted, Runs B702, B703, and B862 through B870, the chromel-alumel thermocouple plug design shown in View B of Fig. 10 was used. For the first two runs, the plugs (of the same material as the nozzle: electrolytic-copper) were seated into place by tightening the nut on the threaded end of the plug. The combination of an inadvertent over-torque on the nuts and the lower strength of the copper at elevated temperature caused the plugs to stretch and eventually to leak exhaust gas past the conical seat. In a revised installation used for the last group of runs, the plug was furnace-brazed to the nozzle at the conical surface and spring-loaded at its outer end. With either of the installations, the thermocouple junction was formed at the copper-to-chrome interface of the 0.003- to 0.005-in. chrome plating which formed the inner surface of the nozzle.

Although the latter installation prevented the occurrence of gas leaks, the junctions opened electrically after only a few tests. It was subsequently determined that the failure resulted from an improper procedure followed in attempting to plate over the exposed thermocouple wire ends. The wire had not been made a part of the plating current path; hence there was not a continuous bond of the layer of chrome over the junction region. Exposure to the high exhaust gas temperature caused the chrome to blister and pull away, breaking the electrical continuity of the junction.

No end-to-end thermocouple calibrations were made throughout the program. However, electrical calibrations of the entire thermocouple amplification and recording system were made for each run. For this procedure, a precision calibration voltage source was substituted for the thermocouple circuit output.

Since the heat transfer computations were based on the transient response characteristics of the recessed chamber thermocouple plug assembly as installed in the chamber, a method of dynamically calibrating the assembly under conditions similar to run conditions was highly desirable. However, means were not available to do this. As an alternative, a qualitative technique to compare the response of individual plugs was developed. The technique consisted of applying a propane/air torch flame to each installed plug at a controlled orientation to the end of the plug and at a constant heat content (mixture ratio and size of flame). The output vs time for the plug was obtained on a recorder, and it was thereby possible to distinguish plugs with a response varying significantly with time or differing from the response of other plugs. Plugs with anomalous behavior were subsequently replaced.

Heat transfer temperatures were recorded on an oscillograph for early runs, but commencing with Run B664 all temperature data were recorded digitally with the MicroSADIC system as previously described.

### C. Combustion Roughness

High-response pressure measurements were made with Photocon water-cooled-diaphragm-type capacitive transducers (Models 342, 345, 307, and 352). After it became evident that mechanical vibration imposed on the transducers when mounted directly to the chamber wall could cause significant electrical output—even transducer destruction—under sufficiently rough combustion conditions, an effort was made to isolate the transducers from these wall vibrations. These efforts were directed primarily towards the use of the Model 352, since it not only was shown to be less vibration sensitive but it also was equipped with a water-cooled flame shield and thus was considered to be the most reliable transducer available for high-response combustion measurements. Of course, it was necessary that the isolated mount retain the essentially flush diaphragm installation that is normally used with the transducer in order to retain high response characteristics.

The soft mount illustrated in Fig. 13 was finally devised and proved to be adequate for the purposes of this program. It is believed that sufficient isolation was achieved to reduce transducer output due to vibration by a factor of from 3 to 10 under the combustion conditions encountered. The isolation characteristics of the mount are discussed further in Ref. 12.

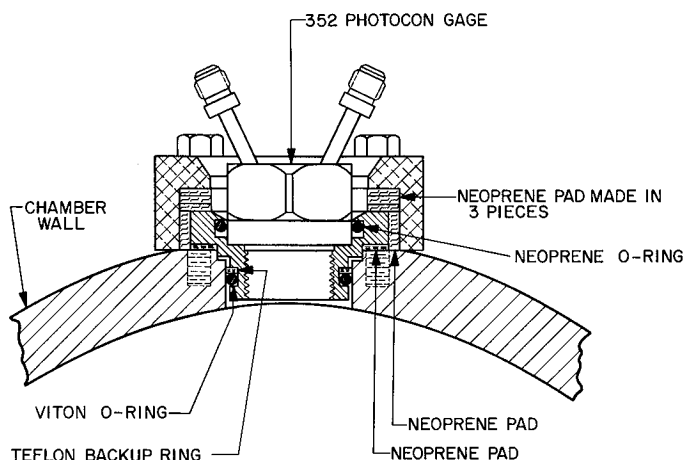


**Fig. 13. Photocon shock mount used in RMIR Program**

Initially, high-response data were recorded (through Run B438) using single- and dual-channel oscilloscope strip film photography. Commencing with Run B411, these data were also recorded directly on a 6-channel Hathaway cathode ray tube (CRT) oscillograph.<sup>13</sup> A CEC 14-channel analog tape recorder<sup>14</sup> became available commencing with Run B465 and, after Run B664, was used exclusively for recording the high-response data. This recorder with some of its associated electronics is shown in Fig. 14.

Since the most meaningful high-response data of the program were obtained using the analog magnetic tape, the high-response system will be described as a system integrated with this device. A typical channel of the system is shown schematically in Fig. 15 and consisted of the Photocon transducer (Model 352, 342, 345, or 307), approximately 450 ft of RG-8/U coaxial transmission cable, Photocon Dynagage (Model DG600, DG400, or DG101) with associated power supplies, Allison Laboratories Model 2-BR filter amplifier,<sup>15</sup> CEC Model 5-752 tape recorder, Kintel Model 111-BF dc amplifier,<sup>16</sup> and Hathaway Model SC-16B or CEC Model S-119-P4 oscillograph. The operating technique was as follows:

- (1) Transducer/transmission cable/Dynagage combination was given static pressure calibration through the appropriate pressure range using the Heise system mentioned in Section III.A. Cooling water flow

<sup>13</sup>Manufactured by Hathaway Instruments, Inc., Denver, Colorado.

<sup>14</sup>Manufactured by Consolidated Electrodynamics Corp., Pasadena, California.

<sup>15</sup>Manufactured by Allison Laboratories, Inc., La Habra, California.

<sup>16</sup>Manufactured by Kintel Division of Cohu Electronics, Inc., San Diego, California.

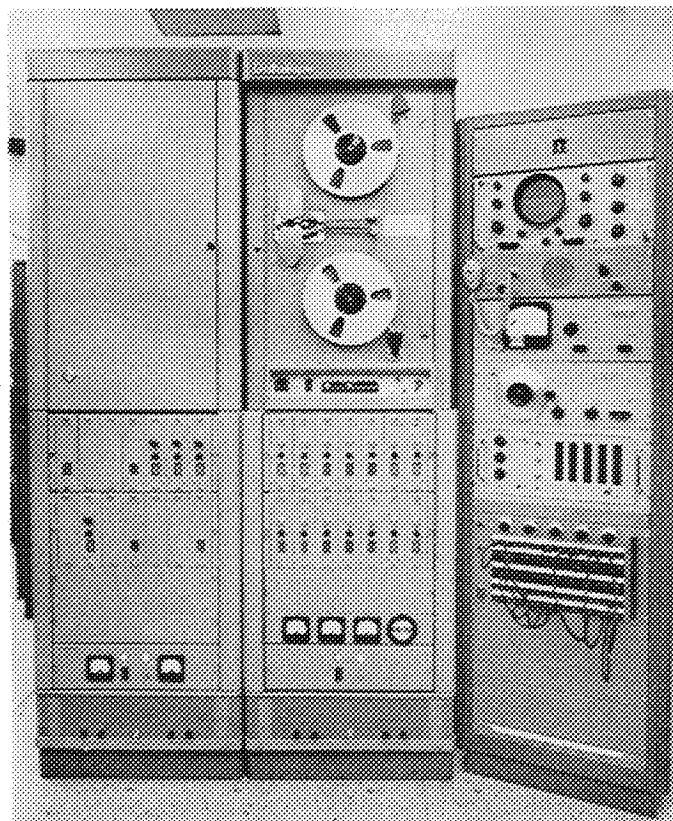


**Fig. 14. Analog tape recorder located in the ETS instrumentation and control center**

was used to improve thermal stability of the transducer.

- (2) Allison amplifier gain was chosen to provide maximum resolution of the expected variations in the ac component of the transducer signal consistent with the tape recorder requirements. If a dc record was also desired, the Allison amplifier was appropriately bypassed.
- (3) Data were recorded on the tape at the maximum record tape speed of 60 ips using the FM mode of the recorder.
- (4) Depending upon the analysis desired, the tape was played back through the Kintel amplifier either at the original 60 ips or at 3¾ ips (slow playback) to the following devices:
  - (a) For dc analog playback records, the dc-coupled tape channel was played back (slow) to the CEC oscillograph with paper speeds available from 1.6 to 100 ips. The recording sensitivity was set

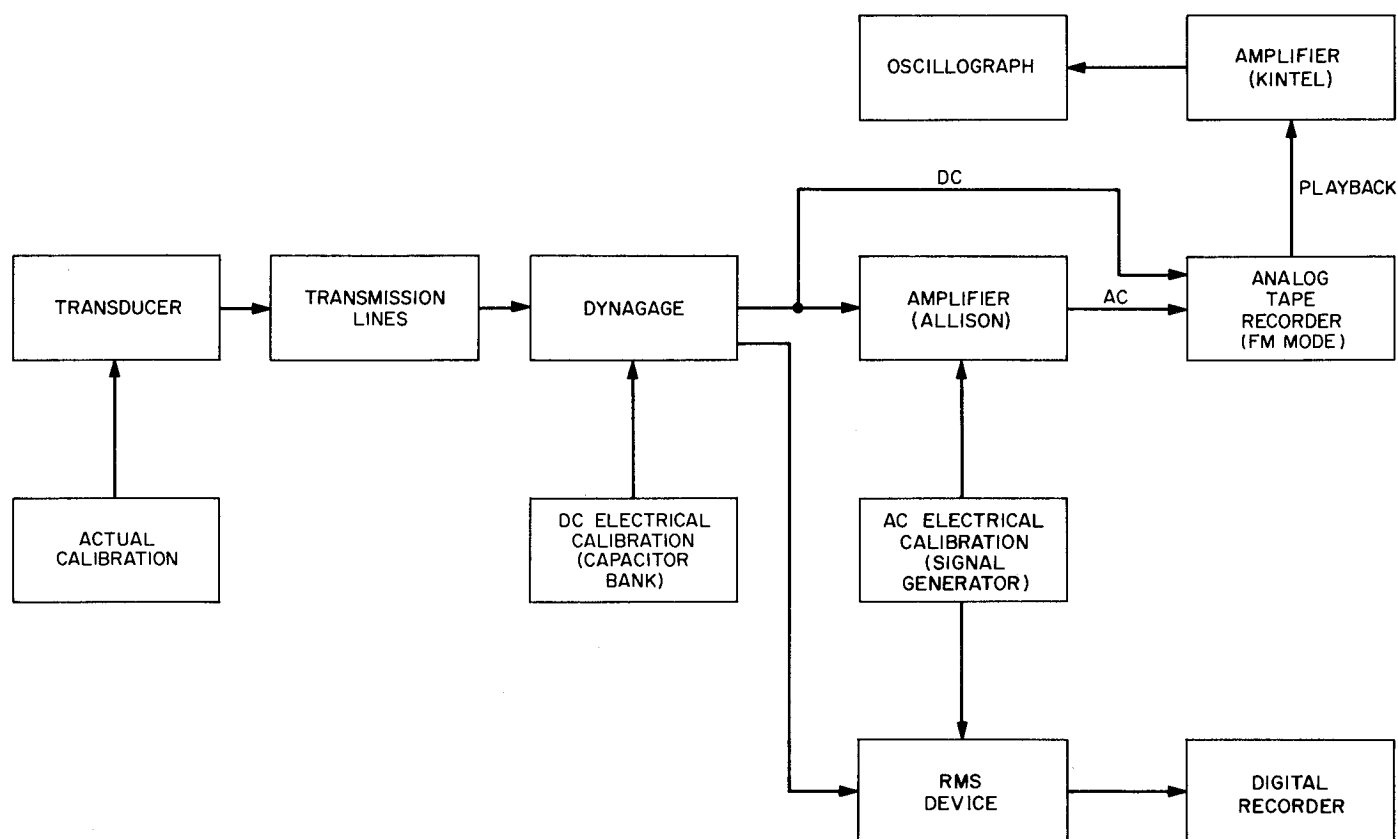


Fig. 15. Block diagram for typical high-response instrumentation channel used in RMIR Program

to provide high-amplitude resolution of the recorded signal. The tape speed reduction factor of 16 allowed the use of relatively low-response (600 Hz) galvanometer elements to record original data with frequency components up to 10 kHz.

- (b) For ac records, either the ac- or dc-coupled (usually ac) tape channel was played back (slow) to the Hathaway oscillograph with any paper speed from 6 to 200 ips. The amplitude resolution was less than that for the CEC oscillograph, but time resolution could be expanded by virtue of the higher available paper speed to approximately 300  $\mu$ sec per inch of record.
- (c) For spectral analysis the tape was played back on another tape and a tape loop was formed. The playback speed to the new tape was selected to provide the proper tape length for the analysis of short-duration runs.

The dynamic amplitude-response of the system just described was evaluated by separately testing the trans-

ducer, signal conditioning, and recording/playback portions of the system. Although each transducer used was not tested, typical units exhibited mechanical resonance in the range of 30 to 40 kHz (depending on the model and pressure rating) when excited on a shock tube, indicating that the mechanical response should be flat ( $\pm 5\%$ ) to at least 8 kHz.

The response of the signal conditioning portions of the system was checked by substituting a Photocon Model FC-110 frequency calibrator (excited with an audio frequency oscillator) for the transducer at the test stand, and evaluating the response at the tape input through the desired range of frequency. The results of these tests showed the following characteristics:

Signal conditioning technique	Response
dc coupling	dc-8 kHz $\pm 5\%$
ac coupling (through Allison amplifier)	100 Hz-8 kHz +0, -5%

Tape system response was determined by recording signals of known amplitude and frequency on the tape at 60 ips and evaluating the output amplitude of the reproduce system at the input to the oscillograph. Thus:

Tape recorder (record through reproduce)	Response
60-ips playback or 3¾-ips playback	dc-8 kHz +0, -8%

Tests were not performed on either of the oscillographs, but the manufacturers specifications are believed to be valid as follows:

Oscillograph/tape playback speed	Response
CEC/60-ips playback	(dc-2500 Hz) ±5%
CEC/3¾-ips playback	(dc-40 kHz) ±5%
Hathaway (ac coupling)/60-ips playback	(10 Hz-80 kHz) ±5%
Hathaway (ac coupling)/3¾-ips playback	(160 Hz-1.2 MHz) ±5%

Thus, making a worst-case estimate by assuming the foregoing response tolerances to be additive, or, where appropriate, controlled by the portion of the system with the narrowest frequency band, the overall amplitude response of the high-response pressure measurement system is estimated to be:

Technique	Overall response
dc-coupled tape recording	
Reproduced on CEC at 60 ips	dc-2500 Hz ±5%
Reproduced on CEC at 3¾ ips	dc-8 kHz +5, -13%
ac-coupled tape recording	
Reproduced on Hathaway at 60 ips	100 Hz-8 kHz +10, -18%
Reproduced on Hathaway at 3¾ ips	160 Hz-8 kHz +10, -18%

A device found to be helpful in the characterization of noiselike combustion roughness—from the standpoint of providing a mean quantitative value for the amplitude of the roughness—was the “rms device” which is included as a part of the high-response system schematic shown in Fig. 15. In operation, the Photocon transducer output (from the Dynagage) was first passed through a wideband sharp-cutoff passive filter and then monitored with an rms converter. As has already been shown, the Photocon system’s flat response lies within the dc to 8 kHz band, beyond which the output of the Dynagage unit is rapidly attenuated. Thus, in order to restrict the rms data to the usable portion of the Photocon response spectrum, the filter specifications were set for cutoff at a high-frequency limit of 8 kHz, with an attenuation of 40 db at 10 kHz, and at a low-frequency limit of 10 Hz, with 24-db/octave attenuation below that limit. Averaging time-constants of 0.1, 0.3, and 1.0 sec were available, it of course being necessary to choose a time constant shorter than the “steady-state” portion of the firing.

The final high-response system to be described was not “instrumentation” per se but was, none the less, interrelated with the Photocon equipment. The device was known as the “instability gear,” and its function was to monitor a selected Photocon channel and to detect periodic fluctuations in chamber pressure which would signify the onset of resonant combustion modes. In this event, the device provided an electrical signal to initiate run termination. Functionally, the circuit comprised a high-pass filter with a selection of five different low-end cutoff characteristics, an R-C network with eight different time constants, and a thyatron circuit with an adjustable firing level which controlled relays in the test stand control circuits. Thus, the proper selection of these settings and an appropriate calibration of the device, based on the sensitivity of the particular Photocon channel being monitored, furnished automatic run termination for a wide range of undesirable combustion conditions.

#### D. Feed System Behavior

This last category of measurements provided essentially “monitoring” kinds of information on the hydraulic and hydrodynamic behavior of the propellant feed systems. The measurements included tank pressure, injector manifold pressure, and propellant valve opening travel, and when combined with the flow and chamber pressure measurements already discussed, yielded the necessary information to monitor the starting flow transient. A secondary check on the primary flow measurements was also obtained from the observed injector pressure drop since all injectors were water-calibrated similarly to the flowmeters.

Starting transient data were obtained from strain-gage transducer outputs recorded by galvo-oscillograph, from which, for example, injector manifold transient pressures could be compared with simultaneously recorded flow rates and valve opening rates. (An elaboration on these procedures is contained in Ref. 7.)

Thus, while this category of information was not used directly for establishing the combustion behavior of particular injectors, it was essential from an operational point of view.

## IV. Computational Methods

### A. Performance

Through run B-664, all performance data were reduced from the strip chart records and computed manually at 0.5-sec intervals throughout each run. The data from subsequent runs (which utilized the digital recording system) were reduced and performance was computed by IBM 7090 computers.

As previously mentioned, for the latter method of computation the digital recording format was compatible with the computer input requirements so that the digital tape could be used directly for input to the computers. Non-linear calibration tables (primarily thermocouple and venturi meter calibrations), propellant physical properties, and the computational programs were introduced from punched cards.

Whether the computations were accomplished manually or by machine, however, they were based on the following standard relationships:

Characteristic velocity  $c^*$ :

$$(c^*)_{1,5} = \frac{A_t g_c (p_{c_{eff}})_{1,5}}{\dot{m}_{ox} + \dot{m}_f} \quad (\text{ft/sec}) \quad (1)$$

where:

$A_t$  = nozzle throat area, in.<sup>2</sup>

$g_c$  = constant of proportionality in Newton's second law of motion, taken as 32.174 lbf ft/lbf sec<sup>2</sup>

$\dot{m}_{ox,f}$  = mass flow rate of oxidizer and fuel, respectively, lbf/sec, computed from the standard venturi meter flow equation:

$$\dot{m} = C_d A_r (2 g_c \rho \Delta p)^{1/2} \quad (2)$$

where

$C_d$  = discharge coefficient (combined velocity and contraction coefficients)

$A_r$  = venturi throat area, ft<sup>2</sup>

$\rho$  = density of flowing medium, lbf/ft<sup>3</sup>

$\Delta p$  = venturi pressure drop (velocity head) psf

$p_{c_{eff}}$  = "effective" chamber pressure equivalent to the isentropic stagnation pressure at the nozzle throat, psia, computed from Ref. 13:

$$(p_{c_{eff}})_1 = \frac{\tilde{p}_{c1} + p_a}{C_1} \quad (3a)$$

$$(p_{c_{eff}})_5 = \frac{\tilde{p}_{c5} + p_a}{C_5} \quad (3b)$$

where the subscripts 1 and 5 refer to the head end and nozzle entrance stations of the chamber, respectively, and

$\tilde{p}_{c1}$  = average of the two head end pressure measurements, psig

$\tilde{p}_{c5}$  = average of the two nozzle inlet pressure measurements, psig

$p_a$  = atmospheric pressure, psia

$$C_5 = \left[ \frac{1}{1 + \left( \frac{\gamma - 1}{2} \right) M_5^2} \right]^{\gamma/\gamma - 1}$$

$$C_1 = C_5 (1 + \gamma M_5^2)$$

$M_5$  = Mach number of combustion gases at inlet to nozzle

$\gamma$  = ratio of specific heats based on a "frozen flow" assumption

Specific impulse  $I_s$ , lbf-sec/lbfm:

$$I_s = \frac{F}{\dot{m}_{ox} + \dot{m}_f} \quad (4)$$

where

$F$  = measured axial thrust, lbf

Thrust coefficient  $C_F$ :

$$(C_F)_{1,5} = \frac{F}{A_t (p_{c_{eff}})_{1,5}} \quad (5)$$

Mixture ratio  $r$  and oxidizer mass fraction  $\phi$ :

$$r = \frac{\dot{m}_{ox}}{\dot{m}_f}$$

$$\phi = \frac{\dot{m}_{ox}}{\dot{m}_{ox} + \dot{m}_f} = \frac{r}{r + 1}$$

## B. Heat Transfer

As described in Section III, temperature-vs-time records were obtained at given engine stations for radial positions 0.020 in. away from the inner wall surface and at the outer wall surface. Using these temperature histories and the initial temperature distribution between the two points as boundary conditions, and "inputting" the known temperature-dependent thermal properties of the wall material, the solution of the radial transient conduction equation for a homogeneous hollow cylinder provided the complete temperature distribution between the two points as a function of time.

This equation may be expressed as:

$$\rho c_p \frac{\partial T}{\partial t} = \frac{\partial}{\partial R} \left( k \frac{\partial T}{\partial R} \right) + \frac{k}{R} \frac{\partial T}{\partial R}$$

where:

$\rho$  = density

$c_p$  = specific heat

$T$  = temperature

$t$  = time

$k$  = thermal conductivity

$R$  = radius

While this equation has no known analytical solution, a solution is closely approximated by using standard numerical methods to transform the differential equation into a difference equation which can then be solved on a digital computer. A derivation of the pertinent difference equation as well as a detailed discussion of the stability criteria and an evaluation of the accuracy of the numerical solution technique is contained in Ref. 11.

Having obtained the temperature distribution between the measurement points in the above manner, it was necessary to extrapolate the distribution across the 0.020-in. recessed distance of the inner thermocouple to obtain the temperature gradient at the inner wall surface,  $(\partial T / \partial R)_w$ . A polynomial extrapolation was used for this purpose.

Instantaneous values of local heat flux at the inner wall were then computed from the Fourier-Biot equation:

$$q = k \left( \frac{\partial T}{\partial R} \right)_w$$

## V. Analysis of Measurement and Computational Accuracy

### A. Sources of Error

Practically all of the measurements of the RMIR Program were obtained under severe environmental conditions characterized by high temperature, corrosive media, mechanical vibration, short test duration and nonsteady operation. Some of the problems of temperature and vibration have already been mentioned in regard to the high-response measurements. Corrosive propellants and erosive combustion gases were potential damaging agents to the heat transfer thermocouple plugs. And short-duration runs and nonsteady operation required reasonably high response of even the performance measurement parameters. Therefore, an assessment of the accuracy of any of the various measurements made in the experiments should account for those errors attributable to the environment and amplitude response requirements as well as the more common errors in experimental measurements such as those associated with calibration, electrical transmission, recording, and readout techniques.

However, estimates of the first-mentioned class of errors sufficiently precise to be meaningful to a quantification of engine performance uncertainty are nearly impossible in the case where the *overall* error is presumed to be of small magnitude. Since it is those firings with relatively small overall error which are of primary interest in this program, we restrict the analysis that follows to apply only to those firings exhibiting so-called smooth combustion and a duration of at least 1.5 sec. Thus, at least the question of gross mechanical vibration and transient operation effects will be avoided.

The static calibrations of the pressure transducers were subject to the usual uncertainties of accidental, fixed, and operational errors, as were the thrust calibrations. However, considerable effort was expended in the development of procedures for the latter, with the result that thrust and pressure calibrations were accomplished with comparable accuracy.

It would have been desirable to have calibrated the flowmeters with actual propellants, but in lieu of this,

standard water calibration data correlated with Reynolds number were used to deduce propellant flow rates. Consequently, the original water calibration errors and errors of the subsequent conversion from water flow to propellant flow combined with the run measurement errors to establish the overall flow measurement accuracy.

The elemental errors introduced by the electronic components of the measurement systems (the amplifiers, power supplies, transmission lines, filters, and recorders) were, in general, relatively small. However, the large number of these components comprising the instrumentation systems increases their total error contribution to significant levels. Thus, these errors will also be considered.

## B. Analysis of Overall Measurement Accuracy

In the analysis, the following assumptions and conditions are stipulated:

- (1) All elemental errors are normally distributed and hence are compatible with standard statistical treatment regarding precision indexes and the propagation thereof (Ref. 14 and 15).
- (2) All elemental errors are based on 20:1 odds, i.e., 95% probability; hence, the final overall accuracy determination has that probability.
- (3) Digital recording and computation is used; hence, there is no error due to the computational method itself.
- (4) Thermochemical data and the procedure used to determine the conversion factor  $C$  in the  $p_{eff}$  equation are correct. Likewise, the propellant physical properties data are assumed to be correct.
- (5) Interparameter phase shift characteristics (unknown) produced insignificant errors in the computation of performance data.
- (6) Thermocouple conversion tables were correct.

**1. Component errors.** Figure 6 shows the various components of error  $e_1, \dots, e_7$  in a strain-gage instrumentation channel from the sensed parameter to the digitized tape record and is typical for the chamber pressure, thrust, and venturi  $\Delta p$  measurements. These error components are first evaluated by estimating the elemental errors making up each component and then combining them (where appropriate) by the standard "square root of the sum of the squares" technique.

*a. Tap and/or coupling errors  $e_1$ .* These consist of amplitude error when the nature (frequency, amplitude,

wave shape) of the fluctuating components of the measurement exceeds the response capabilities of the coupling/transducer system. However, the system will produce a nearly *average* electrical analog for small-amplitude fluctuations at frequencies beyond the response of the system. It is estimated, therefore, that this analog is a true average of the noise-like fluctuations during stable combustion whenever the rms of the  $p_c$  variations (see Section III) is less than 15 psi. Thus, for this analysis,  $e_1 = \text{nil}$ .

*b. Environmental errors  $e_2$ .* Although the thrust load cells were directly connected to the test stand and were therefore exposed to vibration, their bonded strain-gage construction provided low vibration sensitivity. The pressure transducers used for steady-state measurements were also of bonded strain-gage construction but were further isolated from vibration through the use of teflon-lined flexible coupling lines and/or rubber shock mounts. Thus, noise introduced by mechanical vibration for both pressure and thrust will be assumed to be of small amplitude and to be effectively averaged at the digital recorder input filter (0-10 cps low pass).

Transducers were not exposed to heat radiation from the exhaust gases and were shielded from the direct rays of the sun (the temperature effect of the hot combustion gases in the transducer cavity and coupling lines was shown by experiment to be negligible for the short-duration runs of this program). Thus, temperature errors resulted from the ambient temperature change from the time of electrical shunt calibration to run time, and not from nonuniform transducer case temperature. This temperature change is estimated to have been within  $\pm 5^\circ\text{F}$ . The temperature effect on sensitivity for all the transducers was minimized by compensation circuitry, and was quoted by the respective manufacturers as 0.005% full-scale/ $^\circ\text{F}$  for the  $p_c$  transducers, 0.005% reading/ $^\circ\text{F}$  for the load cells, and 0.01% full-scale/ $^\circ\text{F}$  for the  $\Delta p$  transducers.

Therefore,

$$e_2 \text{ for } p_c = 0.00005 \times \pm 5 \times 500 = \pm 0.1 \text{ psi or } \pm 0.04\% \text{ of run level } p_c$$

$$e_2 \text{ for } \Delta p = 0.0001 \times \pm 5 \times 100 = \pm 0.05 \text{ psi or } \pm 0.06\% \text{ of run level } \Delta p$$

$$e_2 \text{ for } F, \text{ per cell} = 0.00005 \times \pm 5 \times 11,500 = \pm 2.9 \text{ lbf or } \pm 0.03\% \text{ of run level } F$$

*c. Actual calibration error  $e_3$ .* The pressure and thrust calibrations are both affected by the same general sources

of error, but because of different calibration techniques the combined errors are separately evaluated. The component error  $e_3$  will be considered as the error in the parameter equivalent  $\beta$ .

$p_c$  and  $\Delta p$

- (1) Calibrator combined accuracy (linearity, hysteresis, resolution, repeatability) .....  $\pm 0.25\%$
- (2) Transducer
  - Linearity ( $\beta$  determined for near run level) ..... nil
  - Temperature effects (temperature assumed constant during calibration) ..... nil
  - Interconnecting wiring (negligible current flow with high impedance system) ..... nil
  - Combined hysteresis and repeatability ....  $\pm 0.27\%$
  - Excitation (short-term stability) .....  $\pm 0.10\%$
  - Readout (digital voltmeter overall accuracy at 30 mv full scale and 24 mv reading) .....  $\pm 0.033\%$

Thus,  $e_3$  for  $p_c$  and  $\Delta p = \pm 0.38\%$ .

Thrust

- (1) Accuracy of calibration of reference load cell (not NBS calibration) .....  $\pm 0.20\%$ 
  - Uncompensated temperature effects ..... nil
  - Repeatability .....  $\pm 0.15\%$
  - Resolution (readout) .....  $\pm 0.025\%$
- (2) Alignment of calibration rig .....  $\pm 0.10\%$
- (3) Measuring cell/stand assembly
  - Interconnecting wiring ..... nil
  - Temperature effects ..... nil
  - Linearity ( $\beta$  determined for near run level) ..... nil
  - Excitation stability (two channels combined) .....  $\pm 0.14\%$
  - Readout (digital voltmeter, overall accuracy two channels combined) .....  $\pm 0.047\%$
  - Combined repeatability and hysteresis ..  $\pm 0.30\%$

Thus,  $e_3$  for thrust =  $\pm 0.43\%$ .

*d. Electrical calibration error  $e_4$ .*

Repeatability .....  $\pm 0.10\%$

Thus  $e_4 = \pm 0.10\%$ .

*e. Electrical excitation error  $e_5$ .*

Excitation stability (from prerun electrical calibration through run) .....  $\pm 0.10\%$

Thus,  $e_5 = \pm 0.10\%$ .

*f. Amplifier error  $e_6$ .*

Amplifier stability (from prerun electrical calibration through run)

Gain .....  $\pm 0.10\%$   
 Linearity (calibrate step applied for near run level) ..... nil  
 Balance .....  $\pm 0.01\%$

Thus,  $e_6 = \pm 0.10\%$ .

*g. Digital recorder error  $e_7$ .*

Resolution .....  $\pm 0.055\%$   
 Short-term stability (from prerun calibration through run) .....  $\pm 0.10\%$   
 Linearity (run level near calibration level) .... nil  
 Electrical noise (combined effects of entire system) .....  $\pm 0.10\%$

Thus,  $e_7 = \pm 0.15\%$ .

**2. Propagation of component errors through performance computations.** The propagation of the above components of error through the data reduction and thermochemical performance calculations will be evaluated as either absolute uncertainties ( $u$ ) or as relative uncertainties ( $U$ ) in the computed results by application of the following relationships (Ref. 14):

$$u_Y = \frac{e_Y Y}{100} \quad (6)$$

$$u_X = \left[ \left( \frac{\partial X}{\partial Y_1} \right)^2 u_{Y_1}^2 + \left( \frac{\partial X}{\partial Y_2} \right)^2 u_{Y_2}^2 + \cdots + \left( \frac{\partial X}{\partial Y_n} \right)^2 u_{Y_n}^2 \right]^{1/2} \quad (7)$$

$$U_X = 100 \frac{u_X}{X} \quad (8)$$

where

$Y$  = the nominal value of a particular measurement ( $p_c$ ,  $\Delta p$  or  $F$ );  $u_Y$  and  $e_Y$  denote the quantification of the error in that measurement.



$X$  = a particular function which is computed from several measurements;  $Y_1, Y_2, \dots, Y_n$ .

The reduction of the digitized performance measurements to engineering units is accomplished using the following equations:

$$p_c \text{ and } \Delta p = \beta_{p_c, \Delta p} \left( \frac{\theta - \theta_{ia}}{\theta_c - \theta_i} \right)_{p_c, \Delta p} = \beta_{p_c, \Delta p} \left( \frac{\Delta \theta}{\Delta \theta_c} \right)_{p_c, \Delta p} \quad (9)$$

$$\begin{aligned} F &= \beta_F \left[ \left( \frac{\theta - \theta_{ia}}{\theta_c - \theta_i} \right)_1 + \left( \frac{\theta - \theta_{ia}}{\theta_c - \theta_i} \right)_2 \right]_F \\ &= \beta_F \left[ \left( \frac{\Delta \theta}{\Delta \theta_c} \right)_1 + \left( \frac{\Delta \theta}{\Delta \theta_c} \right)_2 \right]_F \end{aligned} \quad (10)$$

where:

$\beta$  = parameter equivalent of electrical calibrate step for respective measurement expressed in appropriate engineering units, e.g., psi for  $p_c$  and  $\Delta p$ , and lbf for  $F$ .

$\theta$  = digitized run data (per scan), counts

$\theta_c$  = digitized calibration step (averaged over approximately 127 scans), counts

$\theta_i$  = digitized precalibrate step zero (averaged over approximately 127 scans), counts

$\theta_{ia}$  = digitized prerun zero (averaged over 10 scans just prior to engine start sequence), counts

The thrust reduction equation is considered in this form since the measurement was made with two load cells acting in parallel. The cell outputs were independently recorded; however, the parameter equivalent  $\beta$  was based on the *combined* output of the two cells.

The application of Eqs. (7) and (8) to Eqs. (9) and (10) yields the relative uncertainties in the reduction of the digital data. Thus, for  $p_c$  and  $\Delta p$ ,

$$U_{p_c} = [(U_\beta)_{p_c}^2 + (U_{\Delta \theta_c})_{p_c}^2 + (U_{\Delta \theta})_{p_c}^2]^{1/2} \quad (11)$$

and

$$U_{\Delta p} = [(U_\beta)_{\Delta p}^2 + (U_{\Delta \theta_c})_{\Delta p}^2 + (U_{\Delta \theta})_{\Delta p}^2]^{1/2} \quad (12)$$

and for thrust (taking the cell outputs, calibrate steps, and error sources for the two independently recorded load cell channels to be equal),

$$U_F = \left[ (U_\beta)_F^2 + \frac{1}{2} (U_{\Delta \theta_c})_F^2 + \frac{1}{2} (U_{\Delta \theta})_F^2 \right]^{1/2} \quad (13)$$

Since (from the previously evaluated component errors)

$$U_\beta = e_3 = \pm 0.38\% \text{ for } p_c \text{ and } \Delta p, \text{ and } \pm 0.43\% \text{ for } F$$

and<sup>17</sup>

$$\begin{aligned} U_{\Delta \theta_c} &= [(e_2)^2 + (e_4)^2 + (\text{recorder resolution})^2]^{1/2} \\ &= \pm 0.12\% \text{ for } p_c, \pm 0.13\% \text{ for } \Delta p, \text{ and } \pm 0.12\% \text{ for } F \end{aligned}$$

and

$$\begin{aligned} U_{\Delta \theta} &= [(e_5)^2 + (e_6)^2 + (e_7)^2]^{1/2} \\ &= \pm 0.21\% \text{ for } p_c, \Delta p \text{ and } F \end{aligned}$$

Then, substituting these values in Eqs. (11), (12), and (13) produces:

$$U_{p_c} = \pm 0.45\%$$

$$U_{\Delta p} = \pm 0.45\%$$

$$U_F = \pm 0.49\%$$

Comparison of these uncertainties with those listed in Table 3 shows somewhat greater errors than were desired, but still they are of creditably small magnitude and can be considered as conservatively estimated.

Now, in accordance with Eq. (2), the firing flow rates ( $\dot{m}_{ox}$  and  $\dot{m}_f$ ) were computed from the measured  $\Delta p$ 's, propellant densities based on measured temperatures, and coefficients of discharge based on the familiar Reynolds number correlation. From Eqs. (2), (7), and (8), the uncertainty in the individual flow rate determination is<sup>18</sup>

$$U_{\dot{m}} = \left[ (U_{c_d})^2 + \left( \frac{U_\rho}{2} \right)^2 + \left( \frac{U_{\Delta p}}{2} \right)^2 \right]^{1/2} \quad (14)$$

<sup>17</sup>Note that the recorder, excitation, and amplifier stability errors are presumed to be nil during the calibration portion of the record since the duration of the electrical calibration process is less than 2 sec. Noise error is also nil owing to the averaging technique.

<sup>18</sup>The throat diameter measurement is presumed to have a negligible effect on the final accuracy of flow measurement since the same area is used in computing run data that is used in the flowmeter calibration computations.

Since the propellant physical properties data are assumed to be correct as was previously noted,  $U_p$  depends only on the accuracy of the propellant temperature measurement. If the temperature error is estimated to be  $\pm 2^\circ F$ , an analysis of the density data for the various propellants used in the program produces

$$U_p = \pm 0.14\%$$

As previously mentioned, the uncertainty  $U_{c_d}$  originates in the water calibration of the venturi, the calibration  $c_d$  being computed on the basis of measurement of  $\Delta p$ , average flow rate into a catch tank, and water temperature. The detailed analysis of the flow calibration and Reynolds number correlation errors are not given here but the result of such an analysis yields

$$U_{c_d} = \pm 0.31\%$$

Substituting the appropriate values just determined into Eq. (14) produces, therefore,

$$U_{\dot{m}} = \pm 0.41\%$$

Having determined the major contributing errors, their propagation through the performance calculations can be evaluated. From Eqs. (1), (2), (7), (8), and the substitution of  $\pi D_t^2/4$  for  $A_t$ ,  $U_{c^*}$  can be expressed as

$$U_{c^*} = \left[ (2U_{D_t})^2 + 10^4 \left( \frac{u_{p_c}^2 + u_{p_c'}^2 + 4u_{p_a}^2}{(p_c + p_c' + 2p_a)^2} \right) + \left( -\frac{rU_{\dot{m}_{ox}}}{r+1} \right)^2 + \left( -\frac{U_{\dot{m}_f}}{r+1} \right)^2 \right]^{1/2} \quad (15)$$

and  $U_{I_s}$  can be expressed as

$$U_{I_s} = \left[ (U_F)^2 + \left( -\frac{rU_{\dot{m}_{ox}}}{r+1} \right)^2 + \left( -\frac{U_{\dot{m}_f}}{r+1} \right)^2 \right]^{1/2} \quad (16)$$

and  $U_{c_F}$  can be expressed as

$$U_{c_F} = \left[ (U_F)^2 + 10^4 \left( \frac{u_{p_c}^2 + u_{p_c'}^2 + 4u_{p_a}^2}{(p_c + p_c' + 2p_a)^2} \right) + (2U_{D_t})^2 \right]^{1/2} \quad (17)$$

where

$D_t$  = measured nozzle throat diameter

$p_c' = p_c$  and of two static pressure measurements at the nozzle entrance station of the engine.

Finally, substituting the following values in Eqs. (15), (16), and (17) yields the overall uncertainty in the experimental performance.

$$U_F = \pm 0.49\%$$

$$U_{D_t} = \pm 0.05\% \text{ (estimated)}$$

$$u_{p_c} = u_{p_c'} = \pm 1.35 \text{ psi } (0.45\% \times 300 \text{ psig})$$

$$u_{p_a} = \pm 0.05 \text{ psi (estimated)}$$

$$p_c = p_c' = 300 \text{ psig (nominal chamber pressure)}$$

$$p_a = 13.5 \text{ psia (nominal ETS condition)}$$

$$r = 1.0 \text{ (assumes } \dot{m}_{ox} = \dot{m}_f)$$

$$U_{\dot{m}_{ox}} = U_{\dot{m}_f} = U_{\dot{m}} = \pm 0.41\%$$

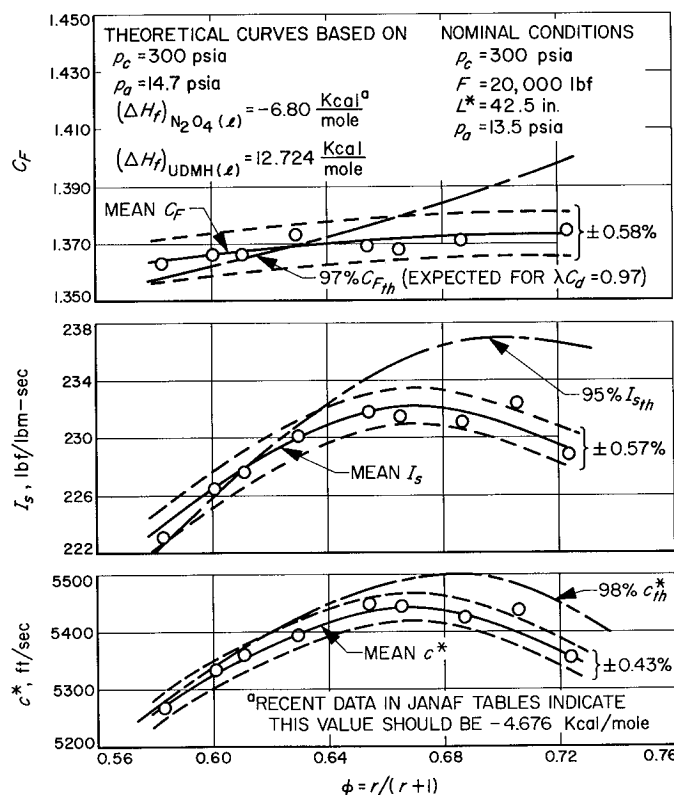


Fig. 16. Experimental performance for RMIR Injector 7 with  $N_2O_4$  plus UDMH

Therefore,

$$U_{c*} = \pm 0.43\%$$

$$U_{I_s} = \pm 0.57\%$$

$$U_{c_F} = \pm 0.58\%$$

For obvious reasons, it is difficult to verify the validity of these estimates of accuracy. Their credibility is enhanced, however, by the comparison of experimental data with theoretical data shown in Fig. 16. The experimental results are from a typical series of smooth firings to determine the thermochemical performance (uncorrected for heat loss) of RMIR Injector 7 over a range of gross mixture ratio. The "scatter" in the data generally falls well

within the computed error limits and the absolute level of performance approaches but never exceeds the computed theoretical values.

Thus, it is concluded that the uncertainty in determining the steady-state performance of the various engines of this program is of the order of 1%. It is recalled, however, that the error analysis presented here does not account for such systematic-error sources as uncertain thermochemical and physical properties data for the propellants or uncertainties in the analytical model used for the computation of effective chamber pressures. The results, therefore, are even more applicable to the resolution of differences in performance between one engine and another than to the determination of absolute level of performance.

## Nomenclature

$A_t$	nozzle throat area, in. <sup>2</sup>	$X$	analytical function computed from several measurements: $Y_1, Y_2, \dots, Y_N$
$A_v$	venturi flow meter throat area, ft <sup>2</sup>	$Y$	nominal value of a particular measurement in appropriate units
$c^*$	characteristic velocity, ft/sec	$\beta$	parameter equivalent in engineering units of particular interest
$c_p$	specific heat at constant pressure, Btu/(lbm-°F)	$\gamma$	ratio of specific heats
$C$	ratio of static to effective chamber pressure (see Section IV)	$\varepsilon_e$	nozzle expansion area ratio
$C_d$	discharge coefficient	$\varepsilon_c$	nozzle contraction area ratio
$C_F$	thrust coefficient	$\theta$	digitized run data, counts
$D_t$	nozzle throat diameter, in.	$\theta_c$	digitized calibration step, counts
$e$	component error, %	$\theta_i$	digitized precalibration zero, counts
$F$	thrust, lbf	$\theta_{ia}$	digitized prerun zero, counts
$FM$	turbine flowmeter output frequency, pulse/sec	$\lambda$	nozzle divergence loss factor
$g_c$	constant of proportionality in Newton's second law of motion, 32.174 (lbm-ft)/(lbf-sec <sup>2</sup> )	$\rho$	density, lbm/ft <sup>3</sup>
$I_s$	specific impulse, (lbf-sec)/lbm	$\sigma$	standard deviation
$k$	thermal conductivity, (Btu-in.)/(in. <sup>2</sup> -sec-°F)	$\phi$	oxidizer mass fraction
$L^*$	characteristic length of combustion chamber, in.	<b>Subscripts</b>	
$\dot{m}$	mass rate of flow, lbm/sec	$a$	ambient
$M$	Mach number	$c$	chamber (except for $g_c$ and $\theta_c$ )
$p$	pressure, lbf/in. <sup>2</sup>	$f$	fuel
$p_{c_{eff}}$	effective chamber pressure, lbf/in. <sup>2</sup> (see Section IV)	$inj$	injector
$\Delta p$	pressure drop across venturi meter, lbf/ft <sup>2</sup>	$ox$	oxidizer
$q$	heat flux, Btu/(in. <sup>2</sup> -sec)	$t$	tank or total (except for $A_t$ and $D_t$ )
$r$	propellant mixture ratio	$w$	wall
$R$	radius, in.	1	injector end of chamber (except when used to designate one of a set of quantities)
$t$	time, sec	5	nozzle end of chamber (except as above)
$T$	temperature, °F	<b>Superscripts</b>	
$u$	absolute uncertainty in engineering units of particular interest	$\sim$	denotes average of two individual measurements
$U$	relative uncertainty, %	'	denotes second of two individual measurements

## References

1. Rupe, J. H., *The Liquid Phase Mixing of a Pair of Impinging Streams*, Progress Report 20-195, Jet Propulsion Laboratory, Pasadena, Calif., August 6, 1953.
2. Rupe, J. H., *A Correlation Between the Dynamic Properties of a Pair of Impinging Streams and the Uniformity of Mixture-Ratio Distribution in the Resulting Spray*, Progress Report 20-209, Jet Propulsion Laboratory, Pasadena, Calif., March 28, 1956.
3. Rupe, Jack H., *An Experimental Correlation of the Nonreactive Properties of Injection Schemes and Combustion Effects in a Liquid-Propellant Rocket Engine: Part I. The Application of Nonreactive-Spray Properties to Rocket-Motor Injector Design*, Technical Report 32-255, Jet Propulsion Laboratory, Pasadena, Calif., July 15, 1965.
4. Rupe, Jack H., *An Experimental Correlation of the Nonreactive Properties of Injection Schemes and Combustion Effects in a Liquid-Propellant Rocket Engine: Part III. On the Relation Between Gross Performance Level and Injection Scheme*, Technical Report 32-255, Jet Propulsion Laboratory, Pasadena, Calif. (to be published).
5. Jaivin, George I., Rupe, Jack H., and Clayton, Richard M., *An Experimental Correlation of the Nonreactive Properties of Injection Schemes and Combustion Effects in a Liquid-Propellant Rocket Engine: Part IV. Relating Heat Transfer to the Chamber Wall and the Injection Pattern*, Technical Report 32-255, Jet Propulsion Laboratory, Pasadena, Calif. (to be published).
6. Rupe, Jack H., *An Experimental Correlation of the Nonreactive Properties of Injection Schemes and Combustion Effects in a Liquid Propellant Rocket Engine: Part V. On the Influence of Vanes on Combustion and Combustion Stability*, Technical Report 32-255, Jet Propulsion Laboratory, Pasadena, Calif. (to be published).
7. Clayton, R. M., and Rupe, J. H., *An Experimental Correlation of the Nonreactive Properties of Injection Schemes and Combustion Effects in a Liquid-Propellant Rocket Engine: Part VI. The Relation Between the Starting Transient and Injection Hydraulics*, Technical Report 32-255, Jet Propulsion Laboratory, Pasadena, Calif., October 29, 1965.
8. Rupe, Jack H., *An Experimental Correlation of the Nonreactive Properties of Injection Schemes and Combustion Effects in a Liquid-Propellant Rocket Engine: Part VII. The Performance Characteristics of Injection Schemes Utilizing High-Flow-Rate Elements*, Technical Report 32-255, Jet Propulsion Laboratory, Pasadena, Calif. (to be published).
9. Nerheim, N. M., *An Experimental Correlation of the Nonreactive Properties of Injection Schemes and Combustion Effects in a Liquid-Propellant Rocket Engine: Part VIII. On the Experimental Performance of the Pentaborane-Hydrazine Propellant Combination*, Technical Report 32-255, Jet Propulsion Laboratory, Pasadena, Calif., April 30, 1962 (Confidential).
10. Inskeep, J., *Dynamic Testing of Pressure Transducers—A Progress Report*, Technical Report 32-268, Jet Propulsion Laboratory, Pasadena, Calif., December 6, 1961.

## References (contd)

11. Powell, Walter B., Howell, Glen W., and Irving, James P., *A Method for the Determination of Local Transient Heat Flux in Uncooled Rocket Motors*, Technical Report 32-257, Jet Propulsion Laboratory, Pasadena, Calif., July 1, 1962.
12. Rogero, R. S., *Measurement of the High-Frequency Pressure Phenomena Associated with Rocket Motors*, Technical Report 32-624, Jet Propulsion Laboratory, Pasadena, Calif., May 11, 1964.
13. Van de Verg, N., and deVorkin, H., *An Investigation of the Influence of Rocket Chamber Configuration on Performance*, Progress Report 1-82, Jet Propulsion Laboratory, Pasadena, Calif., June 4, 1952.
14. Worthing, A. G., and Geffner, J., *Treatment of Experimental Data*, John Wiley and Sons, Inc., New York, New York, 1943.
15. Kline, S. J., and McClintock, F. A., "Describing Uncertainties in Single-Sample Experiments," *Mechanical Engineering*, January 1953, pp. 3-8.

## Acknowledgment

While many individuals contributed significantly to the experimental phases of the RMIR program, the authors would like particularly to acknowledge the efforts of Edward L. Little, whose initiative and conscientiousness as lead technician for the test stand were outstanding. The invaluable instrumentation engineering support of Charles Hammett (formerly of this Laboratory) and Joe Newnham is also recognized.